Rate equation description of a photon gas in a box

—

Beschreibung eines Photonen-Gases im Potentialtopf durch Ratengleichungen

Bachelor thesis in physics

written by

Kelvin Jonathan Küster

at the Department of Physics of the
Rheinland-Pfälzische Technische Universität Kaiserslautern Landau



Supervisor: Priv.-Doz. Dr. Axel Pelster

Second reviewer: Prof. Dr. Georg von Freymann

Handed in on September 14, 2026

Abstract

With the first experimental realization of photon condensation in 2010 in an experiment from the University of Bonn within a dye-filled microcavity at room temperature, interest in the field grew rapidly. Moving on from the original harmonic trapping, this thesis studies the numerics of a photon condensate within a box potential. To this end, a short introduction to the experimental set-up is given. Following this, the Photon Bose-Einstein condensate (BEC) is described for both the closed and open system using rate equations. For the former, this yields the Bose-Einstein distribution known from statistical physics, for the latter an open-dissipative Bose-Einstein distribution emerges. First, the closed system is described by an analytical approximation gained using periodic boundary conditions. This introduces the concept of an infra-red (IR) cut-off. Following this, the closed system numerics are compared for periodic and Dirichlet boundary conditions. This is achieved using the critical particle number of the system. In addition, the numerics then are compared to the analytics to study the IR cut-off and its finite-size behavior. After this, the numerics of the open-dissipative system are introduced which consider Dirichlet boundary conditions. Introduced to the numerics are cavity losses, non-radiative losses and pump parameters. Starting off an analytical fit of the Einstein-coefficients using the Kennard-Stepanov relation is calculated. Next the conditions for convergency of the numerics are analyzed. Lastly, the open-dissipative numerics are used to analyze the chemical potential, as well as the behavior of the critical particle number for the system depending on cavity and non-radiative losses.

Zusammenfassung

Mit der ersten Realisierung eines Photonen-Bose-Einstein-Kondensats (BEK) durch ein Experiment in 2010 an der Universität Bonn wuchs das Interesse an diesem Themengebiet stetig an. Das ursprüngliche Experiment benutzt eine harmonische Falle gefüllt mit Farbstoff, welcher die Photonen thermalisieren lässt. Diese Bachelorarbeit befasst sich mit der Numerik einer Abwandlung dieses Experiments, welches ein Kastenpotential verwendet. Durch eine kurze Einführung in den experimentellen Aufbau, sowie eine theoretische Beschreibung des Photonen BEKs mittels Ratengleichungen für das geschlossene und offene System wird eine Grundlage für numerische Beschreibungen gegeben. Für das geschlossene System mündet dies in der Bose-Einstein-Verteilung, die aus der Statistik bekannt ist. Das offene System fügt dieser zusätzlich einen dissipativen Term hinzu. Zuerst wird das geschlossene System mittels einer analytischen Approximation, gewonnen aus periodischen Randbedingungen, beschrieben. Diese führt das Prinzip eines Infra-rot (IR) cut-off ein. Es folgt danach die Numerik für periodische sowie Dirichlet-Randbedingungen im geschlossenen System, welche miteinander anhand einer kritischen Teilchenzahl verglichen werden. Zusätzlich wird die Numerik des geschlossenen Systems mit der Analytik verglichen, um den IR cut-off und dessen Kastenlängenabhängigkeit zu analysieren. Anschließend wird die Numerik der Ratengleichungen für das offen-dissipative System eingeführt. Dies geschieht unter Dirichlet Randbedingungen. Berücksichtigt werden nun zusätzlich Verlust- und Pumpparameter. In diesem Zug wird mittels der Kennard-Stepanov-Beziehung ein analytischer Fit der Einstein-Koeffizienten kreiert. Folgend liegt der Fokus auf der Konvergenzbedingung der Numerik. Schlussendlich wird anhand dieser Numerik das chemische Potential, sowie das Verhalten des Systems für verschiedene Strahlungs- und nicht-strahlende Verluste mittels der kritischen Teilchenzahl untersucht.

Contents

1 Introduction **1**

2 Rate equation description **3**
2.1 Cavity photon-dispersion and paraxial approximation . . . 3
2.2 Single-particle quantum mechanics . . . 5
2.2.1 Stationary Schrödinger equation . . . 5
2.2.2 Dirichlet boundary conditions . . . 5
2.2.3 Periodic boundary conditions . . . 6
2.3 Quantum statistics . . . 7
2.3.1 Thermal DeBroglie-wavelength . . . 7
2.3.2 Ideal quantum gas and Bose-Einstein distribution . . . 8
2.4 Rate equations . . . 10
2.4.1 Derivation of Bose-Einstein distribution . . . 10
2.4.2 Kennard-Stepanov relation . . . 10
2.4.3 Introducing loss parameters . . . 11
2.4.4 Open-dissipative Bose-Einstein distribution . . . 12
2.4.5 Closed system limit . . . 13
2.5 Summarized conditions for Bose-Einstein condensation . . . 13

3 Closed system **16**
3.1 Analytical approximation for thermal particles . . . 16
3.2 Numerical description . . . 20
3.2.1 Periodic boundary conditions . . . 20
3.2.2 Dirichlet boundary conditions . . . 24
3.3 Calculations for IR cut-off . . . 27

4 Open dissipative system **29**
4.1 Open dissipative approach . . . 29
4.2 Analytical fit of Einstein coefficients and cavity losses . . . 29
4.3 Numerical convergence . . . 31
4.4 Open-dissipative chemical potential . . . 34
4.5 Influence of cavity losses on critical particle number . . . 35
4.6 Non-radiative losses . . . 35

5 Summary and outlook **37**

References **41**

List of figures **43**

1 Introduction

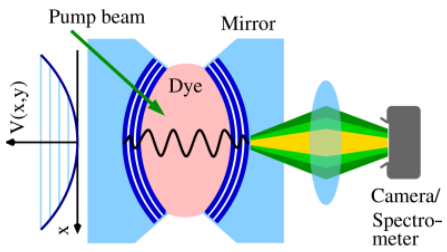
With the turn of the 20th century and the fundamental ideas of quantum physics starting to take root, many new properties of subatomic particles came to light. One of these new found properties was the so called 'spin', a quantized angular momentum of a particle. It was needed explain phenomena like the anomalous Zeeman-effect. An experimental verification of spin existing was later given by Otto Stern and Walther Gerlach with their experiment in 1922 [8]. Furthering this, Wolfgang Pauli introduced the Spin-statistics theorem which dictates that all particles possessing a spin fall into the groups of bosons, if their spin quantum number is an integer, or fermions, if their spin quantum number is that of a half integer [7, 14]. Instead of the classical Boltzmann-distribution, fermions follow the Fermi-Dirac-distribution and bosons behave according to the Bose-Einstein-distribution, yielding different occupational and particle exclusive phenomena [7].

As this thesis deals with results of the Bose-Einstein distribution (BE distribution), firstly it should be explained why it is named after these two historical figures. The initial intention of Bose was to derive Plancks black body radiation formula in a way that is not dependent on any prior classical assumption [1], which lead him to a new particle distribution for bosons. As the Indian Bose wanted to publish his findings in a German magazine, meaning in a language he did not speak, the initial connection between the two was Einstein being the translator for his publication. Einsteins name was added to the distribution due to him using Boses approach and applying it to massive particles within his theory on ideal gases [5]. With this he predicted the phenomenon of a macroscopic ground-state energy level occupation, the famous Bose-Einstein condensation, for bosonic and massive atomic particles in 1925.

The condensation within such a system sets in, when the two different length scales of the mean free path d of a particle in a gas and its thermal DeBroglie-wavelength $\lambda_{\text{th}} \propto (M \cdot T)^{-1}$ which is proportional to the inverse of the temperature T and mass M of the particle, coincide [7]. A particle of light, a photon, is a boson with the integer spin $s = 1$ but misses the thermalizational properties and mass needed for Bose-Einstein condensation. Currently, two experimental set ups are used to bypass these issues by coupling the photons to a thermal bath, either realized with a dye filled micro cavity [12] in which the dye molecules act as a bath for the photons by absorbing and reemitting them or with a vertical cavity surface emitting laser (VCSEL) [16, 18] where the electron-hole-pairs which are allowed to recombine and thus reemit photons due to a driving current fulfill this role [16]. The following chapters will deal with the former case. These cavity set ups consist of a pumping laser, highly reflective mirrors as shown in Fig. 1.1a) and as stated earlier the dye molecules needed to thermalize the photons, resulting in an effective photon mass and a nonlinear dispersion which are needed for condensation. The mirrors create a two-dimensional potential with Fig. 1.1a) showing the case of a harmonic trap. Experimental measurements are taken by a camera depicted in Fig. 1.1a). One mirror is designed so that a few photons can leave the cavity, which in turn then hit the camera lense. A measurement prior to condensation can be seen in the upper panel of Fig. 1.1b). The lower energy photons gather in the middle (colorwise seen in red, orange and yellow light) with their energy rising as they are measured further away from the center (colorwise seen in green light) with the set in of condensation being seen in the lower panel. Most surprisingly, unlike atomic BECs, that need to be cooled down to a few hundred nano Kelvin, a photonic BEC can be created at room temperature [2]. The motivation behind creating a photon BEC within a box trap is that the harmonic confinement results in a spatially inhomogeneous particle density distribution which makes it impossible to determine systematically quantities like the isothermal compressibility $\kappa_T \propto \partial_\mu n$ where μ denotes the chemical potential and n the local particle density systematically [2].

By studying the occupation of thermal and ground states within a photon BEC, the aim of this thesis is to gain an understanding of the critical particle number N_c at which condensation sets in, and the behavior of the BEC under a variation of different parameters like cavity losses or pumping strength. In prior work a set of rate equations is used which describe the experimental system in its entirety. These are used to solve the numerics of the harmonic trap [13], serving as the basis for later numerics, whereas this approach is further applied in the present thesis to a box potential.

a)



b)

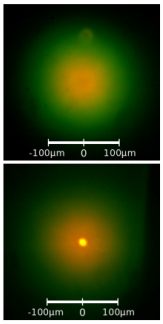


Fig. 1.1: **a)** Scheme of experimental set up regarding a harmonic trapping potential [12]. **b)** Images of spatial radiation distribution transmitted through a single mirror both below (upper panel) and above (lower panel) criticality, showing a macroscopically occupied TEM00-mode for the latter case [12].

Added to that, the numerics resulting from the rate equations of the system and the experiment are also compared to possible analytical approaches. The main intention of the thesis is to work out a proper numerical foundation which describes the experimental box trap [2] that can also be used to test analytics, yielding a more thorough understanding of a photon BEC in a box.

2 Rate equation description

With this section, it is the aim to lay a solid theoretical foundation upon which the later shown problems and results can be discussed. First the experimental set-up will be introduced and the photon dispersion within the cavity is derived. After this a brief derivation of the energy-states considered for the system is given followed by a quantum-statistical section introducing the thermal DeBroglie-wavelength and the Bose-Einstein distribution. The rate equation description of the problem then finalizes the theoretical necessities together with a brief summary of the conditions having to be met for condensation to occur.

2.1 Cavity photon-dispersion and paraxial approximation

Historically an experimental realization of a photon BEC was first succeeded in 2010 using a pumping laser and a dye filled microcavity [12]. Here, a similar setup is considered besides exchanging the harmonic trap in favor of a box potential as can be seen in Fig. 2.1.
The dye molecules are trapped using two cavity mirrors. One of them is constructed to form the walls and the bottom of the box and the other serves as a lid to the box seen in Fig. 2.1. The term "like" is chosen here deliberately, since the experimental box potential is far from the ideal theoretical case of an infinitely high and infinitely steep potential. This is due to it increasing from a ground-level energy floor to a finite value V_0 over a finite space, seen in Fig. 2.1 in the sketch of the left box mirror [6]. This poses two issues for the box length L used for numerical calculations:

1. as the potential V created by the box is not infinite the photon wave function can penetrate the potential wall,
2. V increases over a finite length ($\approx 3.5\,\mu\text{m}$ [6]).

Comparisons between numerics and experiment need to be done while keeping these issues in mind. Following this, consider the photon dispersion relation within a medium [6]

$$E = \frac{\hbar k c}{\tilde{n}}, \tag{2.1}$$

where $\hbar$ denotes the reduced Planck-constant, c is the speed of light and $\tilde{n}$ stands for the refractive index of the dye solution. Fig. 2.1 shows that the wave-vector $\vec{k}$ is to be treated differently in the xy-plane and along the z-axis. This is due to the high anisotropy of the set up as the box depth $\Delta_z \approx 1\,\mu\text{m}$ [6] and $\Delta_x = \Delta_y = L$ are an order of magnitude apart. The underlying concept is called the paraxial approximation. Consider $\vec{k} = \frac{q\pi}{r}$ where q is the longditudinal wave number and r is the length of the box in a given direction. This result is formally derived in the next section under the topic of Dirichlet boundary conditions. The length of the cavity in x and y direction is set as L. For the z direction, the mirrors are subject to surface roughness [6], meaning that instead of $r_z = \Delta_z = \text{const.}$ there is a local variance in mirror distance $\Delta_z = \Delta_{z_0} - \Delta(x,y) = \Delta_z(x,y)$ with $\Delta(x,y) \geq 0$. This is illustrated in Fig. 2.2. As for all $x, y : L \gg \Delta_z(x,y)$ it follows that for all $x, y : k_z = \frac{q\pi}{\Delta_z(x,y)} \gg k_x, k_y$ which is needed to approximate the wave-vector as

$$k = \sqrt{k_x^2 + k_y^2 + k_z^2} = k_z \sqrt{\frac{k_x^2 + k_y^2}{k_z^2} + 1} \approx k_z + \frac{k_x^2 + k_y^2}{2k_z}\,. \tag{2.2}$$

This is a first order Taylor expansion and the core of the paraxial approximation. Using the photon dispersion relation (2.1) together with (2.2), the equation

$$E \approx \frac{\hbar c}{\tilde{n}} \left[\frac{q\pi}{\Delta_{z_0} - \Delta(x,y)} + \frac{k_x^2 + k_y^2}{2q\pi} \cdot (\Delta_{z_0} - \Delta(x,y)) \right] \tag{2.3}$$

results. Within this, the effective mass

$$M_{\text{eff}} = \frac{q\hbar\pi\tilde{n}}{c\Delta z_0} \tag{2.4}$$

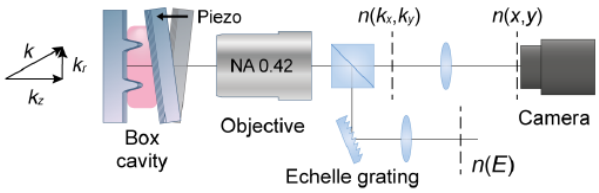


Fig. 2.1: Sketch of dye filled microcavity and measurement instruments [6].

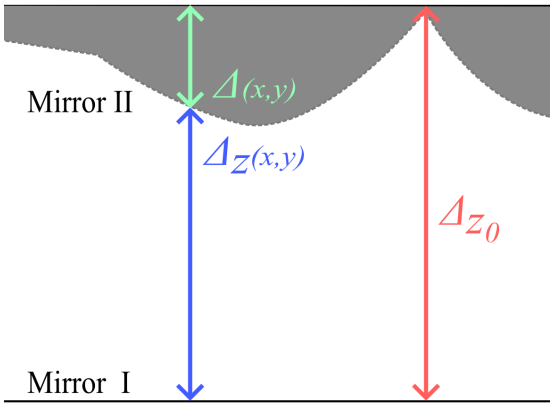


Fig. 2.2: Sketch of the on site dependent mirror distance. Note here that actually both mirrors are subject to surface roughness, meaning $\Delta(x, y)$ is defined in such a way that conceptually elevations from both mirrors are added together and imposed upon mirror two, thus considering mirror one plane.

can be identified yielding

$$\boxed{E \approx M_{\text{eff}} \left(\frac{c}{\tilde{n}}\right)^2 + \frac{\hbar^2(k_x^2 + k_y^2)}{2M_{\text{eff}}} + \frac{M_{\text{eff}}^2}{q\pi\hbar} \left(\frac{c}{\tilde{n}}\right)^3 \Delta(x, y)} \tag{2.5}$$

in first order, consistent with the energy relation of a two-dimensional massive particle. Notably, when introducing this effective mass an effective potential in the linear and quadratic term in M_{eff} appears which introduces a non-zero energy floor to the system. For typical experimental parameters $q = 7$, $\Delta_{z_0} = 1\,\mu\text{m}$ and $\tilde{n} = 1.44$ (refractive index for rhodamine 6G solved in ethylene glycole) this results in an effective photon mass of $M_{\text{eff}} = 7.8 \cdot 10^{-36}$ kg $\approx m_{\text{e}} \cdot 10^{-5}$ with m_{e} as the electron mass [6].

2.2 Single-particle quantum mechanics

The basis of all of the following sections are quantum-mechanics and the inherent quantum-attributes of particles. Deriving the energy eigenstates within a box potential is the first step of understanding the quantum many-particle behavior for such a system. Here this is done considering two different boundary conditions which are later compared to each other in their accuracy of describing the experimental system.

2.2.1 Stationary Schrödinger equation

A single particle within an arbitrary potential has to satisfy the stationary Schrödinger equation (SSE) [19]

$$\hat{H}\psi(\vec{r}) = E\psi(\vec{r}) \tag{2.6}$$

where E is the energy of the particle, $\hat{H}$ is the Hamiltonian and $\psi(x)$ represents the specific wave function of the particle in real space. For a particle in an such a potential the Hamiltonian can be expressed as

$$\hat{H} = \frac{\hat{\vec{p}}^2}{2m} + V(\hat{\vec{r}}) \tag{2.7}$$

$$\hat{\vec{p}} = -i\hbar\nabla_{\vec{r}} \tag{2.8}$$

$$\hat{\vec{r}} = \vec{r} \tag{2.9}$$

with V being the potential the particle is trapped in, m being its mass, $\hat{\vec{p}} = -i\hbar\nabla$ the linear momentum operator and $\hat{\vec{r}} = \vec{r}$ the position operator in the position space. Motivated by the paraxial approximation in the prior section, a two-dimensional system needs to be considered as the z-axis is assumed to be suppressed. This in turn gives

$$\vec{r} = (x,\, y)^{\mathrm{T}} \tag{2.10}$$

$$\hat{\vec{p}} = -i\hbar(\partial_x,\, \partial_y)^{\mathrm{T}} = -i\hbar\nabla_{\mathrm{2D}} \tag{2.11}$$

as the two-dimensional momentum and position operators. For such a box, the potential V is given by

$$V(x,\, y) = \begin{cases} 0,\ 0 \leq x \leq L \text{ and } 0 \leq y \leq L \\ \infty,\ \text{otherwise} \end{cases} \tag{2.12}$$

with L representing the length of the box, which here is equal in each direction.

2.2.2 Dirichlet boundary conditions

For a two-dimensional wave function $\psi(x,\, y)$ Dirichlet boundary conditions impose the equations

$$\psi(\vec{0}) = \psi((x,\, L)) = \psi((L,\, y)) = \psi((L,\, L)) = 0 \tag{2.13}$$

onto the to the systems corresponding wave function. To solve the SSE under these conditions, a seperation ansatz can be employed. With this the wave function $\Psi(x,\, y)$ can be rewritten as two separate functions

$$\psi(x,\, y) = CX(x) \cdot Y(y). \tag{2.14}$$

Here X is solely a function of x, Y solely a function of y and C a numerical constant so that normalization is given. Following this, (2.13) can be applied to both functions individually yielding

$$X(0) = X(L) = 0 \Rightarrow X(x) = \sin\left(\frac{n_x\pi}{L}x\right) \tag{2.15}$$

$$Y(0) = Y(L) = 0 \Rightarrow Y(y) = \sin\left(\frac{n_y\pi}{L}y\right) \tag{2.16}$$

with $n_x,\, n_y \in \mathbb{N}_{>0}$. Such X and Y conform to (2.13) and (2.14). Neither n_x nor n_y can be equal to zero as normalization would not be satisfied in that case and e.g. $n_x' = -n_x$ would describe the same

quantum state. Plugging (2.15) and (2.16) into (2.6) yields

$$-\frac{\hbar^2}{2m}\nabla_{2D}^2\psi(x,\,y) = \frac{\hbar^2}{2m}\left[n_x^2\left(\frac{\pi}{L}\right)^2 + n_y^2\left(\frac{\pi}{L}\right)^2\right]\cdot X(x)Y(y) = E\cdot X(x)Y(y) \tag{2.17}$$

$$\tag{2.18}$$

which leads to the expression

$$E = \frac{\hbar^2}{2m}(k_x^2 + k_y^2) = \frac{\hbar^2}{2m}|\vec{k}|^2 \tag{2.19}$$

for the energy when identifying

$$k_i = \frac{n_i\pi}{L}. \tag{2.20}$$

Here $i \in \{x, y\}$.

2.2.3 Periodic boundary conditions

Using the seperation ansatz in (2.14) again, the equations

$$X(0) = X(L) \tag{2.21}$$
$$Y(0) = Y(L) \tag{2.22}$$

are imposed on the system, for the given boundary conditions. Using the SSE to solve the problem, the functions

$$X(x) = e^{i\frac{2\pi}{L}n_x x} \tag{2.23}$$
$$Y(y) = e^{i\frac{2\pi}{L}n_y y} \tag{2.24}$$

are applicable solutions to the SSE. Differing by a factor of two to the Dirichlet case (2.20)

$$k_i = 2\pi\frac{n_i}{L}\,, \tag{2.25}$$

$i \in \{x,\, y\}$ can be identified. Note that here $n_x,\, n_y \in \mathbb{Z}$. Similarly to (2.19), the energy of a particle in the specific quantum state can be written as

$$E = \frac{\hbar^2}{2m}\left[\left(2\pi\frac{n_x}{L}\right)^2 + \left(2\pi\frac{n_y}{L}\right)\right] = \frac{\hbar^2}{2m}(k_x^2 + k_y^2) = \frac{\hbar^2}{2m}|\vec{k}|^2 \tag{2.26}$$

which is gained by plugging (2.23) and (2.24) into (2.6).

2.3 Quantum statistics

Having discovered quantum mechanical descriptions of single particle (or small particle number) problems using the Schrödinger-Equation, for example the model of the hydrogen atom can be solved exactly. Bigger molecules like the H_2^+ molecular ion have their behavior described when using approximations. Following this promising start, physicists started introducing quantum mechanical principles to statistical physics. Along this line, the derived energy quanta will be used, together with the particle spin to derive the Bose-Einstein distribution.

2.3.1 Thermal DeBroglie-wavelength

As stated in the introduction, Bose-Einstein condensation occurs when two different length scales coincide for a particle in the gas: the thermal deBroglie wavelength λ_{th} and the mean-free path. As such, to underline the conceptual importance of the former, this part will derive it independently, even though it could also be introduced in the following quantum gas section, as it naturally appears for further calculations.
For a particle confined within an arbitrary volume V and potential $U(\vec{q})$ the classical Hamilton function [7] is

$$H(\vec{q},\vec{p}) = \frac{\vec{p}^2}{2m} + U(\vec{q}) \tag{2.27}$$

resulting in the classical partition function [7]

$$Z = \frac{1}{(2\pi\hbar)^j} \int \mathrm{d}q^3 \int \mathrm{d}p^3 \; e^{-H(\vec{q},\vec{p})/(k_{\mathrm{B}}T)} \; . \tag{2.28}$$

when considering a single particle in three dimensions. Here T is the temperature of the ensemble and the coordinates $\vec{q} = (q_1,\, q_2,\, q_3)$ and $\vec{p} = (p_1,\, p_2,\, p_3)$ are the canonical coordinates of the particles. When plugging (2.27) into (2.28) the equation

$$Z = \frac{1}{(2\pi\hbar)^3} \int \mathrm{d}^3r \; e^{-\frac{U(\vec{r})}{k_{\mathrm{B}}T}} \int \mathrm{d}^3p \; e^{-\frac{p^2}{2mk_{\mathrm{B}}T}} \tag{2.29}$$

results. Looking only at the momentum integration

$$\frac{1}{(2\pi\hbar)^3} \int \mathrm{d}^3p \; e^{-\frac{p^2}{2mk_{\mathrm{B}}T}} = \frac{(\sqrt{2mk_{\mathrm{B}}T})^3}{(2\pi\hbar)^3} 4\pi \int_0^\infty \mathrm{d}x \; r^2 e^{-r^2} = \frac{(\sqrt{2\pi mk_{\mathrm{B}}T})^3}{(2\pi\hbar)^3} = \frac{1}{\lambda_{\mathrm{th}}^3} \tag{2.30}$$

the factor

$$\boxed{\lambda_{\mathrm{th}} = \sqrt{\frac{2\pi\hbar^2}{mk_{\mathrm{B}}T}}} \tag{2.31}$$

known as the thermal deBroglie wavelength can be identified. To solve (2.30) the substitution $r = \frac{p}{\sqrt{2mk_BT}}$ and the identity $\mathrm{d}^3p = 4\pi p^2 \mathrm{d}p$ were used. Using this, (2.28) turns into

$$Z = \int \frac{\mathrm{d}^3q}{\lambda_{\mathrm{th}}^3} e^{\frac{U(\vec{q})}{k_{\mathrm{B}}T}} \tag{2.32}$$

as the dimensionless classical partition function.

2.3.2 Ideal quantum gas and Bose-Einstein distribution

Within statistical mechanics, one of the earliest introduced concepts is that of the ideal gas meaning particles confined in a volume V via boundary conditions with no particle-particle interaction and no inherent particle volume. This approximation can also be looked at under a quantum-statistical lense, with the case of photons being nearly ideal as there is an almost vanishing particle-particle interaction between the quanta and nearly no volume they occupy. Before the underlying physics can be studied, one needs to choose through which statistical ensemble the system should be described by with the options being...

1. ...the micro-canonical ensemble: closed system,
2. ...the canonical ensemble: system in heat exchange with a bath,
3. ...the grand-canonical ensemble: system in heat and particle exchange with a bath.

In the given case of a photon BEC, experimentally the condition $\sum_\nu n_\nu = N$ where n_ν are the particles in each quantum state ν meaning that the particle number N is strictly conserved is difficult, if not impossible to realize. Thus the most fitting description is using the grand-canonical ensemble and its partition function

$$Z_\mathrm{G} = \sum_{N=0}^{\infty} \sum_{\substack{\{n_\nu\} \\ \sum n_\nu = N}} e^{-\beta(E[\{n_\nu\}] - \mu \sum_\nu n_\nu)} \tag{2.33}$$

with the reciprocal temperature $\beta = \frac{1}{k_\mathrm{B} T}$ and μ stands for the chemical potential. It is to be noted that unlike in the earlier classical case, now instead of an integral there is a sum over the quantized energy eigenstates. The sum over $\{n_\nu\}$ indicates every possible permutation of the occupation of the energy states whilst fulfilling the constraint that $\sum n_\nu = N$. The two sums can be combined into a singular one $\sum_{N=0}^{\infty} \sum_{\substack{\{n_\nu\} \\ \sum n_\nu = N}} = \sum_{\{n_\nu\}}$ where there is now no further constraint imposed upon the permutations. For bosons this gives

$$Z_\mathrm{G} = \sum_{\{n_\nu\}} e^{-\beta(E[\{n_\nu\}] - \mu \sum_\nu n_\nu)}. \tag{2.34}$$

The energies can be rewritten as the particles in a state multiplied with the energy of the eigenstate

$$= \sum_{\{n_\nu\}} e^{\sum_\nu (\varepsilon_\nu n_\nu - \mu n_\nu)}. \tag{2.35}$$

This can be expressed as a product of sums

$$= \prod_\nu \underbrace{\left[\sum_n e^{-\beta(\varepsilon_\nu - \mu) n} \right]}_{\text{geometric series}} \tag{2.36}$$

where a geometric series can be employed under the condition that $\mu < \varepsilon_\nu$ for all ν. It should be noted, that this especially includes the ground-state energy ε_0. Finalized, this reads

$$\Rightarrow \boxed{Z_\mathrm{G} = \prod_\nu \frac{1}{1 - e^{-\beta(\varepsilon_\nu - \mu)}}} \tag{2.37}$$

as the expression for the bosonic grand-canonical partition function. This yields the grand-canonical potential

$$\Phi = -\frac{1}{\beta} \ln Z_\mathrm{G} = \frac{1}{\beta} \sum_\nu \ln\left(1 - e^{-\beta(\varepsilon_\nu - \mu)}\right). \tag{2.38}$$

With this, calculating the distribution function is simply a matter of taking the derivative of Φ in regards to μ leaving

$$-\left.\frac{\partial \Phi}{\partial \mu}\right|_T = \boxed{n(\varepsilon_\nu) = \frac{1}{e^{\beta(\varepsilon_\nu - \mu)} - 1}} \tag{2.39}$$

as the final result.

2.4 Rate equations

With (2.39) the mathematical term for the Bose-Einstein distribution is given. Here this result is reproduced using rate equations of e.g. pump driven dye-lasers. This approach allows to naturally introduce loss parameters and thus an open-dissipative Bose-Einstein distribution.

2.4.1 Derivation of Bose-Einstein distribution

Einstein explained [4] that there are three basic processes how a light mode interacts with a two-state system. The first is stimulated absorption in which the ground-state dye molecules M_1 within the cavity absorb a photon and jump to the higher energy state $(1 \to 2)$ of the system which happens at a rate $B_{12}M_1N$ where N denotes the number of photons in the cavity. The excited molecules M_2 can also fall back down to the lower level $(2 \to 1)$ via the process of stimulated emission at a rate $B_{21}M_2N$ and spontaneous emission $A_{21}M_2$ with which a photon is released back into the system in the same mode. As M_1, M_2 and N are dimensionless, B_{12}, B_{21} and A_{21} are rate factors with the unit Hz. They are called Einstein coefficients. These elementary processes do not account for any interaction between the photons and the cavity, meaning loss rates are ignored for now. In steady-state, this yields the rate equation

$$\dot{N} = 0 = \underbrace{B_{21}M_2N + A_{21}M_2}_{2\to1} - \underbrace{B_{12}M_1N}_{1\to2} \tag{2.40}$$

which when using the result $A_{21} = B_{21}$ coming from quantum optics [22] results in

$$N = \frac{1}{\frac{B_{12}M_1}{B_{21}M_2} - \frac{B_{21}M_2}{B_{21}M_2}} = \frac{1}{\frac{B_{12}M_1}{B_{21}M_2} - 1} \,. \tag{2.41}$$

Note that all Einstein coefficients depend on the energy of a state ν, meaning $B_{12} = B_{12}(\nu)$ etc.. To show that (2.39) and (2.41) are equivalent the ratio of stimulated absorption to stimulated emission $\frac{B_{12}M_1}{B_{21}M_2}$, which determines N, has to be rewritten using the Kennard-Stepanov relation.

2.4.2 Kennard-Stepanov relation

In order to properly explain the thermalization of photons within a cavity, this section derives the Kennard-Stepanov relation in a heuristic approach [9,10,20–22]. The system is split up into two electronic energy levels, that of the ground-state and excited molecules. The molecules can however be subject to vibrational (phononic) excitations, meaning for each electronic energy level there also exist different vibrational sublevels. The energy of the transition between purely electronic states is assumed as E_{ZPL}, the zero phonon line energy. The particles occupy the vibrational states according to the Boltzmann distribution

$$P(\Delta E_1) = e^{-\frac{\Delta E_1}{k_\mathrm{B}T}} \tag{2.42}$$

for the lower state sublevels and

$$P(\Delta E_2) = e^{-\frac{\Delta E_2}{k_\mathrm{B}T}} \tag{2.43}$$

for the upper state sublevels. Sought after is now a connection between B_{21} and B_{12}. As the energy within the system is conserved, the equation

$$E_{\mathrm{ZPL}} + \Delta E_2 = E + \Delta E_1 \tag{2.44}$$

has to hold, meaning (2.43) can be expressed as

$$P(\Delta E_2) = P(\Delta E_1) e^{-\frac{E - E_{\mathrm{ZPL}}}{k_\mathrm{B}T}} \,. \tag{2.45}$$

For any given transition at the energy $E+\Delta E_1$ between a lower and higher level vibrational state consider the Einstein coefficient $B_{12}(E, \Delta E_1)$. Under the earlier assumption, that the lower vibrational levels are thermally (Boltzmann) occupied, the total absorption coefficient $B_{12}(E)$ is given by

$$B_{12}(E) = \frac{1}{\hbar} \int \mathrm{d}\Delta E_1 \sigma(\Delta E_1) B_{12}(E, \Delta E_1) P(\Delta E_1) \tag{2.46}$$

with $\sigma(\Delta E_1)$ expressing the density of states within the lower vibrational levels. The integral gives a macroscopic average over all the microscopic $B_{12}(E, \Delta E_1)$. Using the same approach, this results together with (2.45) in

$$B_{21}(E) = \frac{1}{\hbar} e^{-\frac{E-E_{\mathrm{ZPL}}}{k_{\mathrm{B}}T}} \int \mathrm{d}\Delta E_2 \sigma(\Delta E_2) B_{21}(E, \Delta E_2) P(\Delta E_1) \tag{2.47}$$

for the stimulated emission coefficient. Given a two level system, the detailed condition

$$\sigma(\Delta E_1) B_{12}(E, \Delta E_1) = \sigma(\Delta E_2) B_{21}(E; \Delta E_2) \tag{2.48}$$

together with (2.47) yields

$$B_{21}(E) = e^{-\frac{E-E_{\mathrm{ZPL}}}{k_{\mathrm{B}}T}} B_{12}(E). \tag{2.49}$$

This is known as the Kennard-Stepanov relation. It is to be noted that the photon gas thermalizes to the spectral temperature that can be found within the exponent, meaning for any experiment $T = \text{const.}$ has to be fulfilled.
Returning back to equation (2.41), in full now using the Kennard-Stepanov relation (2.49), this turns into

$$N(E_\nu) = \frac{1}{\frac{B_{12}(E_\nu) M_1}{B_{21}(E_\nu) M_2} - 1} = \frac{1}{e^{\beta(E_\nu - \mu)} - 1} \tag{2.50}$$

with which the chemical potential

$$\mu(M_1, M_2) = E_{\mathrm{ZPL}} - \frac{1}{\beta} \ln\left(\frac{M_1}{M_2}\right) \tag{2.51}$$

is defined and gives an equation akin to (2.39). Later it is shown that in conjuncture with the rate equations, this definition of the chemical potential needs loss parameters to be considered in order to be well defined.

2.4.3 Introducing loss parameters

Away from theoretically ideal cases lies the real, experimental world in which it is not possible to have perfect reflection on each mirror or no interaction between the molecules that could lead to photon losses. This however is also a benefit, as within the following section, not only will loss parameters be introduced to a set of rate equations, it will also be shown that they are inherently needed for any form of condensation to occur. Overall, to fully describe the system, a set of three equations is needed; one in regards to the photon number and two for the molecular behavior [3]. Within the cavity, it is expected that the number of molecules does not change, where they may change their energy states but never leave the system. The resulting equation reads

$$M = M_1 + M_2 \tag{2.52}$$

or in terms of rate of change

$$\frac{\partial M_2}{\partial t} = -\frac{\partial M_1}{\partial t} \tag{2.53}$$

where t is time. Realistically there are processes, that can lead to losses in the molecular number, however the time scale on which they happen is way larger than anything needing to be considered in regards to the photon lifetimes, meaning they are irrelevant to the description. Following this, either $\dot{M}_1$ or $\dot{M}_2$ need to be defined to complete the information in regards to the molecular behavior, where here we will use the latter. The only way for a lower state molecule to enter the excited state is by absorbing a photon, which means $\dot{M}_2$ needs to be directly influenced by pM_1 where p denotes the external pumping rate. Leaving the excited state, is possible in two ways, radiative and non-radiative. The latter depends on the (in dye-laser literature) so called fluorescence lifetime [3] t_{F} where its inverse $1/t_{\mathrm{F}} = \Gamma_{\mathrm{nr}}$ is the rate factor at which non-radiative losses happen. The former is the process of stimulated emission giving a

direct contribution to $\dot{M}_2$ by the change of photons $\dot{N}$. Due to the introduction of loss parameters, the cavity losses however here need to be subtracted from the change of photons as they happen independent of any molecular transition of state, resulting in a dependency on $\dot{N} - \Gamma_c N$ with Γ_c being the cavity loss rate. These processes together give the equation

$$\dot{M}_2 = pM_1 - \Gamma_{nr} M_2 - (\dot{N} - \Gamma_c N) \tag{2.54}$$

which just reads as the rate of change of the excited molecules is the pumping of the lower state minus the non-radiative losses minus the rate of change of photons without the cavity losses. To obtain the full description of $\dot{M}_2$, the rate of change of photons now needs to be given. To this end only the consideration of cavity losses has to be introduced into the earlier derived equation (2.40) for $\dot{N}_\nu$ meaning

$$\dot{N}_\nu = [B_{21}(E_\nu)M_2 - B_{12}(E_\nu)M_1 - \Gamma_c(E_\nu)]N_\nu + B_{21}(E_\nu)M_2 \tag{2.55}$$

is the final system equation. Brought together and with $\dot{N}$ plugged into $\dot{M}_2$ from bottom to top, the three rate equations needed to describe the open-dissipative system of a BEC read [3, 13]:

$$\dot{N}_\nu = [B_{21}(E_\nu)M_2 - B_{12}(E_\nu)M_1 - \Gamma_c(E_\nu)]N_\nu + B_{21}(E_\nu)M_2 \tag{2.56}$$

$$\dot{M}_2 = pM_1 - \Gamma_{nr} M_2 - \sum_\nu \{[B_{21}(E_\nu)M_2 - B_{12}(E_\nu)M_1]N_\nu + B_{21}(E_\nu)M_2\} \tag{2.57}$$

$$M = M_1 + M_2 \ . \tag{2.58}$$

This can then be specified for Dirichlet or periodic boundary conditions as needed.

2.4.4 Open-dissipative Bose-Einstein distribution

From this point onward, the rate equations will be examined in steady-state, meaning the system is assumed to be in a quasi equilibrium. This allows for (2.56) to be rewritten in the form

$$N = \frac{B_{21}M_2}{B_{12}M_1 - B_{21}M_2 + \Gamma_c} \tag{2.59}$$

with N,B_{12}, B_{21} and Γ_c all still depending on the energy of a given state. Like (2.41) this can be simplified using the Kennard-Stepanov relation. Mathematically the additional loss term in the denominator can either be absorbed into the chemical potential or left as is, yielding respectively

$$N_\nu = \frac{1}{e^{\beta(E_\nu - \mu_\nu)} - 1} \tag{2.60}$$

with the energy-dependent chemical potential

$$\mu_\nu = E_{ZPL} - \frac{1}{\beta}\ln\left\{\frac{M_1}{M_2}\left[1 + \frac{\Gamma_c(E_\nu)}{B_{12}(E_\nu)M_1}\right]\right\} \tag{2.61}$$

or alternatively

$$N_\nu = \frac{1}{e^{\beta(E_\nu - \mu)} - 1 + \frac{\Gamma_c(E_\nu)}{B_{21}(E_\nu)M_2}} \tag{2.62}$$

with the second interpretation of the energy-independent chemical potential

$$\mu = E_{ZPL} - \frac{1}{\beta}\ln\left(\frac{M_1}{M_2}\right) \ . \tag{2.63}$$

Note that (2.63) and (2.51) are the same, meaning that the difference between the closed and open system lies in the distribution. Now considering a more physical argumentation, an energy dependent chemical potential is in violation of thermodynamics, as for equilibrium between two systems to exists, their chemical potentials need to be equal meaning that for the given system, when disregarding degeneracy, all photon modes would be out of equilibrium and as a result no photon thermalization would take place and no condensate could exist. Thus (2.62), the open-dissipative Bose-Einstein distribution, is at the core of the numerics. In addition, the ratio $\frac{\Gamma_c(E_\nu)}{B_{21}(E_\nu)M_2}$ can also be written as t_e/t_c meaning emission time divided by cavity life-time of a photon. As this ratio is of the order $1 \cdot 10^{-1}$, it has usually been neglected within descriptions of the system [11].

2.4.5 Closed system limit

In numerical simulations it is the luxury that parameters like the cavity losses can be changed within seconds just by swapping out numbers. Thus the question arises as Γ_c and Γ_{nr} can be tweaked at wish, if there is a solution to the rate equations for the limit of $\Gamma_c \to 0$. Approaching this, the rate equations in steady state

$$\dot{N}_\nu = 0 = [B_{21}(E_\nu)M_2 - B_{12}(E_\nu)M_1 - \Gamma_c(E_\nu)]N_\nu + B_{21}(E_\nu)M_2 \tag{2.64}$$

$$\begin{aligned}\dot{M}_2 = 0 &= pM_1 - \Gamma_{nr}M_2 - \sum_\nu \{[B_{21}(E_\nu)M_2 - B_{12}(E_\nu)M_1]N_\nu + B_{21}(E_\nu)M_2\} \\ &= pM_1 - \Gamma_{nr}M_2 - (\dot{N} - \Gamma_c N)\end{aligned} \tag{2.65}$$

are considered. Plugging (2.64) into (2.65) gives

$$0 = pM_1 - \Gamma_{nr}M_2 + \Gamma_c N \tag{2.66}$$

for finite loss parameters. Taking the closed system limit in regards to cavity losses, i.e. $\Gamma_c \to 0$, this leaves

$$p = \Gamma_{nr}\frac{M_2}{M_1} \tag{2.67}$$

and assuming $\Gamma_{nr} = 0$ as the goal is to consider also vanishing non-radiative losses, finally

$$pM_1 = 0 \tag{2.68}$$

is the result. To solve this equation, mathematically the two options of $p = 0$ and $M_1 = 0$ exist. The former poses the physical problem that for no pumping, there also are no photons in the cavity, which of course means that there cannot be a photon BEC. The latter would mean that there is no longer any interaction between photons and molecules leading to thermalization breaking down, another key component in the emergence of a photon BEC. This means that for the closed system limit, the rate-equations have no physical solution.

2.5 Summarized conditions for Bose-Einstein condensation

Now in order to summarize and combine the prior subsections into clear conditions, whether condensation is possible within a given system, one needs to positively answer three questions:

1. is there a ground-state definded within the system,
2. is the photon particle number conserved,
3. is the Bose-gas thermalized?

In the experimental set-up, the mirror-cavity, besides introducing an effective photon mass and quadratic dispersion relation as derived earlier, also defines a ground-state or rather a low-energy cutoff that acts as a ground-state energy level for the photons to which they can condense to, as can be seen in Fig. 2.3 or earlier in Fig. 1.1a). In addition to that, the theoretical derivation of (2.39) shows that only the Bose-Einstein distribution allows for macroscopic occupation of the ground-state energy level. In the thermodynamic limit, as $N \to \infty$ the chemical potential μ approaches the energy ε_0 of the given ground-state within the system, meaning when considering all energy eigenmodes ν, ground-state and thermal particle number need to be treated separately

$$\boxed{N = \sum_\nu n(\varepsilon_\nu) = \sum_\nu \frac{1}{e^{\beta(\varepsilon_\nu - \mu)} - 1} = N_0 + \sum_{\nu \neq 0} \frac{1}{e^{\beta(\varepsilon_\nu - \mu)} - 1}} \tag{2.69}$$

with N_0 now being the diverging term as the particle number within the system increases. This principle is at the core of the following numerics, as their aim is to simulate both the behavior of ground and thermal particles for a given system.

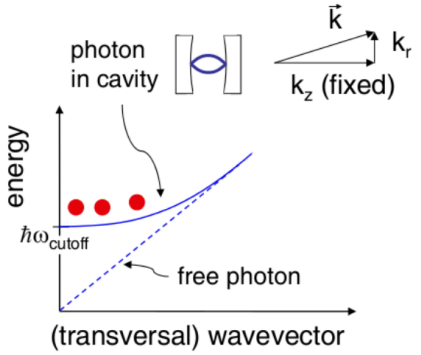


Fig. 2.3: Sketch of low-energy cut-off and quadratic photon dispersion introduced by the cavity. This is contrasted with the linear dispersion of a free photon [23].

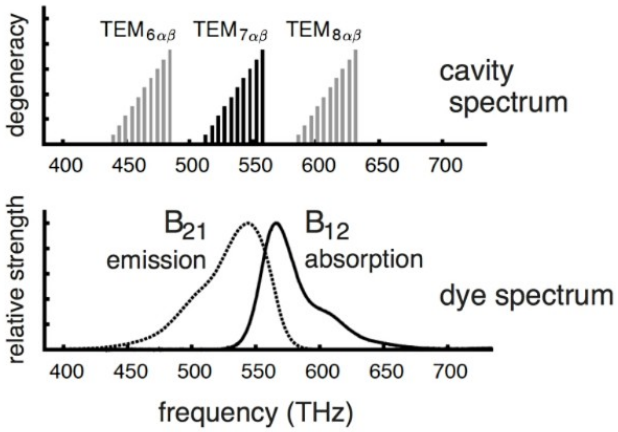
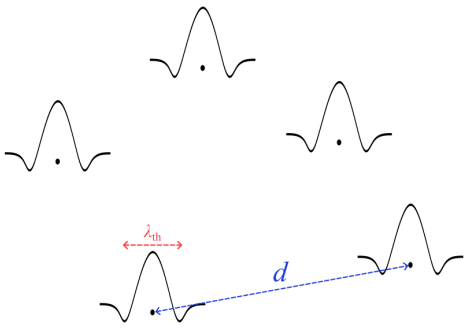


Fig. 2.4: Emission and absorption spectrum using Rhodamine 6G as a dye solution for different transversal wave modes. For TEM_7 the Kennard-Stepanov relation is fulfilled meaning the photons are thermalized within their dye-bath [11].

a)



b)

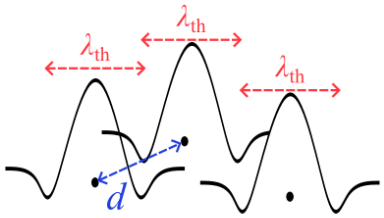


Fig. 2.5: Illustration of the different length scales needed to be considered within a BEC. Case **a)** shows $d/\lambda_{\mathrm{th}} \gg 1$ for which no condensation is possible and case **b)** shows $d/\lambda_{\mathrm{th}} \approx 1$ at which point condensation can occur. Experimentally for a given particle λ_{th} can be tweaked by changing the temperature and the mean free path d can be adjusted by introducing more particles to the system or by taking ones away.

Condition number two is simply given for the closed system, as particle conservation is the inherent definition of it and for the open-dissipative system, the interplay between pumping strength and cavity

losses is tuned in such a way that $\dot{N} = 0$ meaning the experiment is in steady-state. Lastly the third condition of thermalization is less apparent as it comes from the Kennard-Stepanov relation. When deriving (2.49), the only assumption was that the molecules are thermalized within their vibrational states. The photons inherit this thermalization when Kennard-Stepanov is fulfilled where the emission- and absorption-spectrum needed is seen within Fig. 2.4. For the given experiment, this leaves all questions answered positively, meaning photon condensation is to be expected. Adding to that, for the sake of completeness as stated in the introduction, besides the aforementioned questions, a BEC also only occurs once the mean free path between two particles and λ_{th} coincide, where a sketch of this is provided within Fig. 2.5. As $\lambda_{\mathrm{th}} \propto (M \cdot T)^{-1/2}$, when regarding the in (2.5) introduced effective photon mass which is at least nine orders of magnitude smaller than that of an atom, the temperature of the gas can be increased drastically from a few nK for atomic BECs to up to room temperature of 300 K for photon BECs.

3 Closed system

This section deals with the numerical evaluations of the closed system, neglecting all pump and loss parameters. Furthermore, the closed system is evaluated using two different boundary conditions, namely periodic and Dirichlet. This is done to demonstrate that Dirichlet boundary conditions are closer to the experimental set up and therefore better suited to numerically describe the underlying theory of the photon gas. Intuitively the closed system numerics underestimate the critical photon number N_c as there are no photon losses needed to be compensated. All plots and numerical simulations were created using the programming language Python.

3.1 Analytical approximation for thermal particles

Over the course of studying and encountering many given systems in physics, the realization sets in that almost any problem is easiest to understand when looking through the lense of an analytical solution or a suitable approximation. This ease of understanding however does not come without a tradeoff, as for every approximation taken on the way to an analytical result, its accuracy in describing the actual system decreases further and further. Through this view, calculating analytics for the closed system, which is already an approximation of the open dissipative system, as losses Γ_c and Γ_nr are set to zero, might seem like wasted effort at first glance. To address this, the analytical result discussed will be left with a correction constant that can be determined using the closed system numerics to tie analytics and numerics together. The derivation uses periodic boundary conditions due to them being easier to approximate analytically. Starting off, consider the energy of a single particle within a box potential

$$E_{\vec{k}} = \frac{\hbar^2}{2M}|\vec{k}|^2 = \frac{\hbar^2}{2M}k^2 = \frac{\hbar^2}{2M}(n_x^2 + n_y^2) \quad n_x, n_y \in \mathbb{Z} \tag{3.1}$$

using periodic boundary conditions as derived in (2.26). In the two-dimensional k-space, a base is given by the family

$$B = \left(k_1 = \frac{2\pi}{L}\begin{pmatrix}1\\0\end{pmatrix},\ k_2 = \frac{2\pi}{L}\begin{pmatrix}0\\1\end{pmatrix}\right) \tag{3.2}$$

so that

$$\vec{k} = \begin{pmatrix}k_x\\k_y\end{pmatrix} = \frac{2\pi}{L}\begin{pmatrix}n_x\\n_y\end{pmatrix} \tag{3.3}$$

for any given vector $\vec{k}$. Using this discrete vector space, numerically the particle numbers can now be calculated using the BE-distribution from (2.69)

$$\sum_{\vec{k}} N_{\vec{k}} = \sum_{\vec{k}} \frac{1}{e^{\beta(E_{\vec{k}}-\mu)} - 1} \tag{3.4}$$

but as an analytical result is sought after, the next approximation is now to be made. Despite $E_{\vec{k}} \propto k^2$, the energy levels can be considered very close together, an assumption further justified by later numerics, which makes it possible to turn the discrete sum over $\vec{k}$ into an integral. This is done using the Euler-Maclaurin formula

$$\sum_{n_x,n_y} f(n_x, n_y) \approx \int \mathrm{d}n_x \int \mathrm{d}n_y f(n_x, n_y) \tag{3.5}$$

in first order. As the interest lies in the thermal particle number $N_\mathrm{th} = N - N_{\vec{k}=\vec{0}}$, the next approximation is to determine how to best cut out the ground-state photons analytically, meaning an infra-red (IR) cut-off needs to be introduced which is depicted in Fig. 3.1. As the integration boundaries in the k-space are $-\infty$ to $+\infty$ when using the base B, it is easier to shift the calculations into polar coordinates. This has the added benefit of not having to worry about approaching the IR cut-off from negative and positive direction for both k_x and k_y. Taking this into consideration and introducing the currently unspecified IR cut-off k_0, the thermal particle number can be calculated by the integral

$$N_\mathrm{th} = \frac{L^2}{4\pi^2}\int_0^{2\pi}\mathrm{d}\phi\int_{k_0}^{\infty}\mathrm{d}k' \frac{k'}{e^{\frac{\hbar^2 k'^2}{2Mk_\mathrm{B}T} - \frac{\mu}{k_\mathrm{B}T}} - 1} \tag{3.6}$$

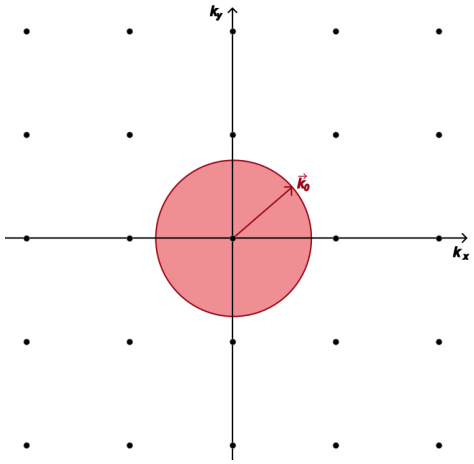


Fig. 3.1: Sketch of the IR-cut off. The red circle depicts a possible volume which is cut out in the k-space to introduce the cut-off, with $|\vec{k_0}|$ being its radius. Each grid point denotes aan energystate that can be occupied by photons.

with the new line element $\frac{L^2}{4\pi}\mathrm{d}\phi\mathrm{d}k'$ being determined using

$$\vec{k} = \begin{pmatrix} k_x \\ k_y \end{pmatrix} \Rightarrow \begin{pmatrix} n_x \\ n_y \end{pmatrix} = \frac{L}{2\pi}\begin{pmatrix} k'\cos\phi \\ k'\sin\phi \end{pmatrix} \tag{3.7}$$

and the Jacobian matrix $J = \frac{L}{2\pi}\begin{bmatrix} \cos\phi & \sin\phi \\ -k'\sin\phi & k'\cos\phi \end{bmatrix}$ and its determinant $\det(J) = \frac{L^2}{4\pi^2}k'$ corresponding to the transformation. The integration over ϕ leaves nothing but a factor of 2π with the k' integral needing to be simplified a bit more. Consider the substitution $x = \frac{\hbar^2 k'^2}{2Mk_\mathrm{B}T} \Rightarrow \mathrm{d}k' = \mathrm{d}x\frac{Mk_\mathrm{B}T}{\hbar^2 k'}$ which can be plugged into (3.6) yielding

$$N_\mathrm{th} = \frac{L^2}{2\pi}\frac{Mk_\mathrm{B}T}{\hbar^2}\int_{x_0}^{\infty}\mathrm{d}x\frac{1}{e^{x-\frac{\mu}{k_\mathrm{B}T}}-1}. \tag{3.8}$$

Still left unspecified, $x_0 = \frac{\hbar^2 k_0^2}{2Mk_\mathrm{B}T}$ is now the dimensionless IR cut-off for the shifted coordinate x. Before calculating further, using the thermal deBroglie-wavelength, the pre-factor to the remaining integral can already be identified with $\frac{L^2}{2\pi}\frac{Mk_\mathrm{B}T}{\hbar^2} = \frac{L^2}{\lambda_\mathrm{th}^2}$. Similar to earlier parts, the geometric series $\frac{1}{1-q} = \sum_{l=0}^{\infty} q^l \quad |q| < 1$ can be employed giving

$$N_\mathrm{th} = \frac{L^2}{\lambda_\mathrm{th}^2}\int_{x_0}^{\infty}\mathrm{d}x\frac{1}{e^{x-\frac{\mu}{k_\mathrm{B}T}}-1} = \frac{L^2}{\lambda_\mathrm{th}^2}\sum_{l=1}^{\infty}\frac{e^{(\frac{\mu}{k_\mathrm{B}T}-x_0)l}}{l}. \tag{3.9}$$

Employing the geometric series is possible due to the constraint $\mu < E_{\vec{k}}$ for all $\vec{k}$ given in the derivation of (2.39). Now the polylogarithm [15]

$$\mathrm{Li}_1(z) = \sum_{l=1}^{\infty}\frac{z^l}{l} = -\ln(1-\mathrm{z}) \tag{3.10}$$

can be identified with the summation over l in (3.9) resulting in

$$N_\mathrm{th} = -\frac{L^2}{\lambda_\mathrm{th}^2}\ln\left(1-e^{\frac{\mu}{k_\mathrm{B}T}-x_0}\right) \tag{3.11}$$

as the wanted expression for the thermal photon number. The IR cut-off x_0 included in the solution can now be transformed to properly understand its purpose. Looking back at the shift into polar coordinates,

having k_0 as the lower boundary to the integral represents cutting out a disc of phase-space area which is assumed to be the area occupied by the ground-state photons. This means, that the edge of that disc fulfills the equation $k_x^2 + k_y^2 = k_0^2$ with k_0 being the radius of the disc. This in return is a basis to set $k_0 = \frac{2\pi}{L}\sqrt{d_0}$ with $d_0 \geq 0$ being a dimensionless constant that allows the radius of the disc to be set. With this the IR cut-off transforms into $x_0 = \frac{\hbar^2(2\pi)^2}{2Mk_\mathrm{B}TL^2}d_0 = \pi\frac{\lambda_\mathrm{th}^2}{L^2}d_0$. To simplify the notation, one can rescale $d_0 = \frac{c_0}{\pi}$ to absorb the factor π left within x_0, meaning the result (3.9) reduces to

$$N_\mathrm{th} = -\frac{L^2}{\lambda_\mathrm{th}^2}\ln\left(1 - e^{\frac{\mu}{k_\mathrm{B}T} - \frac{\lambda_\mathrm{th}^2}{L^2}c_0}\right), \tag{3.12}$$

with the cut-off still being unspecified due to c_0. Due to the definition of d_0, $c_0 \geq 0$ also needs to be fulfilled. Knowing $x_0 \propto 1/L^2$, the cut-off can be interpreted as a finite-size correction, since in the thermodynamic limit ($N \to \infty\,,\quad L^2 = V \to \infty\,,\quad N/V = \text{const.}$) it tends to zero. Overall the result shows, that the thermal photon number depends on the system parameters of the area L^2 of the box trap and the thermal wavelength of the photons which corresponds to their temperature. These can all be experimentally altered. As a variable, only μ remains with c_0 to be individually determined for each system that is to be described with (3.12) in mind. To check for the logical consistency of this result, it would be best to look at a few different values for c_0:

$\underline{c_0 \to \infty}$**:**

First it can be checked whether c_0 does actually fulfill its intended purpose as a scalar of the radius of the cut-out of photons. Consider the upper-bound case of $c_0 \to \infty$, with this

$$N_\mathrm{th} \to -\frac{L^2}{\lambda_\mathrm{th}^2}\ln(1) = 0 \tag{3.13}$$

which is logical, as this case implies that we cut out an ever growing disc in the phase-space, finally leaving no photons to be considered 'thermal'.

$\underline{c_0 = 0}$**:**

The lower-bound case $c_0 = 0$ results in

$$N_\mathrm{th} = -\frac{L^2}{\lambda_\mathrm{th}^2}\ln\left(1 - e^{\frac{\mu}{k_\mathrm{B}T}}\right) \tag{3.14}$$

which does not converge as $\mu \uparrow 0$. Again, this is self consistent as this case implies not cutting out any photons at all, meaning $N_\mathrm{th} = N$ which naturally goes to infinity as N grows.

$\underline{c_0 = 1}$**:**

Lastly, a simple case from which a critical particle number N_c can be derived would be $c_0 = 1$ where

$$N_\mathrm{c} \approx N_\mathrm{th}(\mu = 0) = -\frac{L^2}{\lambda_\mathrm{th}^2}\ln\left(1 - e^{-\frac{\lambda_\mathrm{th}^2}{L^2}}\right). \tag{3.15}$$

This only depends on two experimental parameters. Fig. 3.2 shows the case $N_\mathrm{c} \approx 4817$ for $L = 40\,\mu\mathrm{m}$ and $\lambda_\mathrm{th} = 1.48\,\mu\mathrm{m}$ for the sake of illustration.

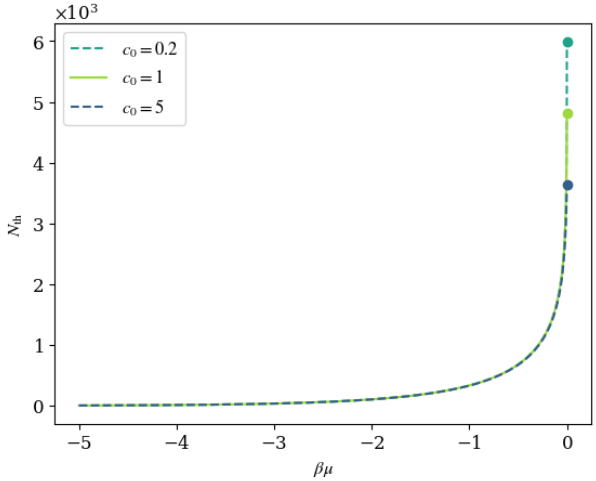


Fig. 3.2: Thermal photon number $N_{\mathrm{th}}(\mu)$ from (3.12) with $L = 40\,\mu\mathrm{m}$, $\lambda_{\mathrm{th}} = 1.48\,\mu\mathrm{m}$ and three different values for c_0. Indicated as a dot at the end of each graph is the critical photon number, which in the case of $c_0 = 1$ yields $N_{\mathrm{c}} \approx 4817$.

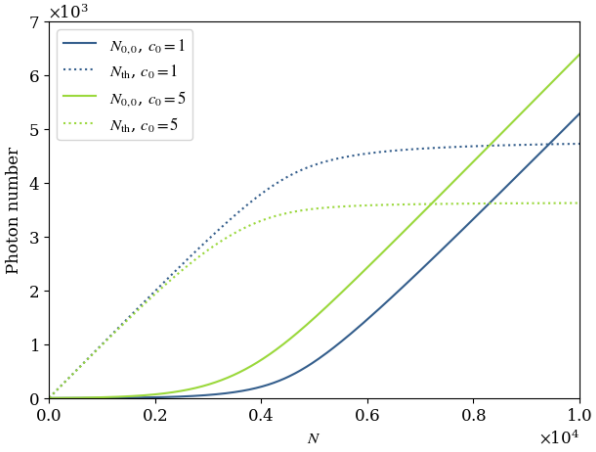


Fig. 3.3: Occupation of ground- and thermal-state particles for different values of c_0 as a function of the total particle number.

It might seem intuitive, but it is also to be noted that as depicted in Fig. 3.2
the behavior of the system as it tends towards criticality is influenced by the choice of c_0 in the way that N_{c} changes. This is further established in Fig. 3.3 which emphasizes that there is a resulting difference in the saturation of the thermal states. As seen in the following parts, the behavior shown in this figure resembles that of the numerically determined curves, giving more credibility to the analytical approach. For now the only remaining question in regards to the analytical solution is how c_0 can be determined using the numerics. Rather straightforward, once N_{c} ist determined numerically, it can be plugged into (3.12), so that $N_{\mathrm{th}} \uparrow N_{\mathrm{c}}$ ($\mu \uparrow 0$) can be used gaining the equation

$$N_{\mathrm{c}} = -\frac{L^2}{\lambda_{\mathrm{th}}^2} \ln\left(1 - e^{-\frac{\lambda_{\mathrm{th}}^2}{L^2} c_0}\right). \tag{3.16}$$

This can be solved for c_0 yielding

$$c_0 = -\frac{L^2}{\lambda_{\mathrm{th}}^2} \ln\left(1 - e^{-\frac{\lambda_{\mathrm{th}}^2}{L^2} N_{\mathrm{c}}}\right) \tag{3.17}$$

as the needed equation to calculate c_0. It is to be noted, that this calculation alone does not give information about how c_0 depends on μ.

3.2 Numerical description

Now shifting away from analytics towards numerics, approaching the problem using the closed system description offers a few benefits. First and foremost, the difficulty in implementation is less, since as known, here the loss parameters Γ_{nr} denoting the non-radiative losses and Γ_{c} meaning the cavity losses are fully ignored. Instead of numerically solving the closed system rate equation (2.40), the Bose-Einstein distribution can be used directly. This is due to the fact that both approaches were shown equivalent when using the Kennard-Stepanov relation as seen in the derivation of (2.50). This is then used to determine particle numbers within the system. This reduction in complexity is a double edged sword, as it reduces the accuracy of the model. In summary, the goal of this section however is not to perfectly describe the experimental system, but to lay a solid foundation upon which the open-dissipative numerics can be studied. As the here considered boundary conditions only differ in the values of the energy and the summation boundaries, it is appropriate to explain the numerical approach here. The BE-distribution is used, to plot both the total particle number N and the ground-state particle number N_{g} as a function of the chemical potential μ. From this, the thermal particles $N_{\mathrm{th}}(\mu)$ are gained simply using the relation

$$N_{\mathrm{th}}(\mu) = N(\mu) - N_{\mathrm{g}}(\mu) \tag{3.18}$$

after which both N_{g} and N_{th} will be plotted against N to determine

$$N_{\mathrm{g}} = N_{\mathrm{g}}(N), \tag{3.19}$$

$$N_{\mathrm{th}} = N_{\mathrm{th}}(N). \tag{3.20}$$

Their behavior is examined for varying box lengths L. The analytically introduced IR cut-off can then be studied. Furthermore, the critical particle number N_{c}, at which condensation sets in, is determined for each length. Here N_{c} is calculated by the fitting function

$$N_{\mathrm{control}} = N - N_{\mathrm{c}}^{\mathrm{fit}} \tag{3.21}$$

for the ground-state particles past condensation. To this end, for each graph only the final values of $N_{\mathrm{g}}(N)$ are used as input for the fitting function, which is then overlayed with the graph of $N_{\mathrm{g}}(N)$ to determine accuracy for $N > N_{\mathrm{c}}$.

3.2.1 Periodic boundary conditions

For the experimental set-up, periodic boundary conditions are the least accurate way of description as they here are used for the closed system and are further removed from the experiment than Dirichlet boundary conditions. Note that in the thermodynamic limit however, differences between both boundary conditions vanish. Nontheless, they are the easiest to calculate and are also used to derive the analytical approximation, meaning that in calculating everything first using periodic boundary conditions a general intuition for the system can be garnered, as well as giving an opportunity to check analytical results in a system closest to the assumptions underlying the derivation. All together, this section will stay mostly surface-level, serving the purpose of properly introducing certain numeric approaches while not diving too deep into a less accurate approach. First the energy eigenstates derived for periodic boundary conditions are taken into account for the BE-distribution. When taking into account (2.50) and (2.26) this results in

$$N = \sum_{n_x,n_y=-\infty}^{\infty} N_{n_x,n_y} = \sum_{n_x,n_y=-\infty}^{\infty} \frac{1}{e^{\frac{2\pi^2\hbar^2}{Mk_{\mathrm{B}}TL^2}(n_x^2+n_y^2)-\frac{\mu}{k_{\mathrm{B}}T}}-1}, \tag{3.22}$$

where now the thermal deBroglie-wavelength from (2.31) can be used to simplify the given equation to

$$N = \sum_{n_x,n_y=-\infty}^{\infty} N_{n_x,n_y} = \sum_{n_x,n_y=-\infty}^{\infty} \frac{1}{e^{\pi\frac{\lambda_{\mathrm{th}}^2}{L^2}(n_x^2+n_y^2)-\frac{\mu}{k_{\mathrm{B}}T}}-1}. \tag{3.23}$$

Thus

$$N = \frac{1}{e^{-\frac{\mu}{k_{\mathrm{B}}T}}-1} + \sum_{\substack{n_x,n_y=-\infty \\ (n_x,n_y)\neq(0,0)}}^{\infty} \frac{1}{e^{\pi\frac{\lambda_{\mathrm{th}}^2}{L^2}(n_x^2+n_y^2)-\frac{\mu}{k_{\mathrm{B}}T}}-1} \tag{3.24}$$

is obtained, with the first term of (3.24) representing the ground-state particles and the second the thermal-state particles. Here however, the low energy cut-off E_{cut} introduced by the box that defines the system ground state is not yet considered. The energy eigenvalues now all shift upwards by this constant value giving

$$\tilde{E}_{\vec{n}} - \mu = E_{\mathrm{cut}} + E_{\vec{n}} - \mu \tag{3.25}$$

where now the cut-off can be absorbed into the chemical potential via

$$\tilde{\mu} = \mu - E_{\mathrm{cut}} \,. \tag{3.26}$$

It is important to differentiate between these two chemical potentials as now $\mu \to E_{\mathrm{cut}}$ $(N \to \infty)$ and $\tilde{\mu} \to 0$ $(N \to \infty)$ differ in their behavior towards the thermodynamic limit. Considering this, N and N_{g} can be plotted against the shifted chemical potential $\tilde{\mu}$ where a sharp increase in particle occupation is expected close to the ground-state energy $E_{0,0} = 0$ as confirmed in Fig. 3.4.

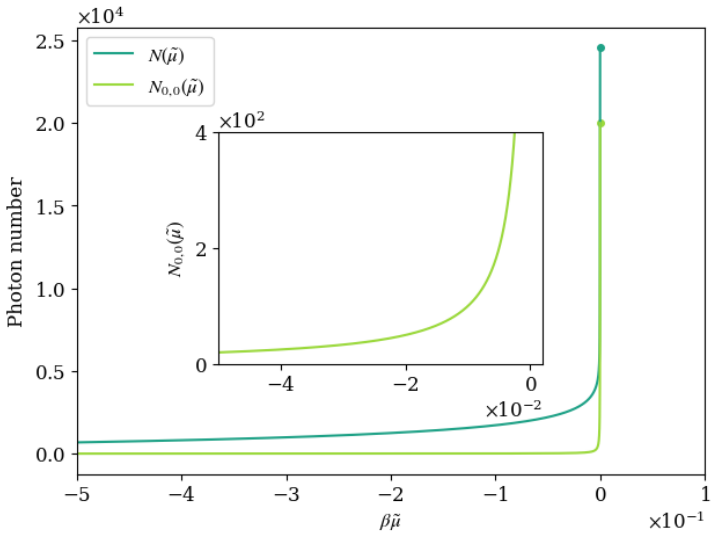


Fig. 3.4: Total particle number N and $N_{0,0}$ plotted against $\beta\tilde{\mu}$ using the experimental parameters $L = 40\,\mu\mathrm{m}$, $T = 300\,\mathrm{K}$ and $\lambda_{\mathrm{th}} = 1.48\,\mu\mathrm{m}$. The large points at the end of each graph denote the final value obtained before the singularity at $\beta\tilde{\mu} = \beta E_{0,0}$. The inset depicts the behavior of $N_{0,0}$ close to criticality showing that the behavior of the ground state and overall particles is largely similar besides occupation of the former starting at a smaller $\beta\tilde{\mu}$.

As the expected behavior of the thermal particles is saturation at the value of N_{c}, Fig. 3.4 allows for an initial estimate of the critical particle number to be made. This is done by calculating $N_{\mathrm{th}} = N - N_{0,0}$ for $\tilde{\mu}$ very close to the ground-state energy. For the depicted endpoints in the graph, this comes out to

$$N_{\mathrm{c}} = N_{\mathrm{th}}^{\mathrm{sat}} \approx 4582 \tag{3.27}$$

where $N_{\mathrm{th}}^{\mathrm{sat}}$ stands for the saturation level of the thermal particles. Fig. 3.4 was created considering a maximum $n_{\mathrm{max}} = 100$ of modes defined by

$$n_{\mathrm{max}} \geq |n_x| \,,\ |n_y| \tag{3.28}$$

meaning it is the largest quantum number needed to be considered in each direction for the sum to converge. It should also be stated, that for every following graph if not explicitly stated differently, the same values of temperature and thermal wavelength are used. Using the explained linear fit in (3.21), Fig. 3.5a) depicts a critical particle number $N_{\mathrm{c}} = 4550$ which is equal to the converged value shown in Fig. 3.5b) and in good agreement with the initial estimate of $N_{\mathrm{th}}^{\mathrm{sat}} = 4582$. The expected saturation of thermal particles as well as the linear character of the ground-state particles for large N can be seen. To check for self-consistency of the numerics, it can also be looked at whether the same N_{c} can be garnered

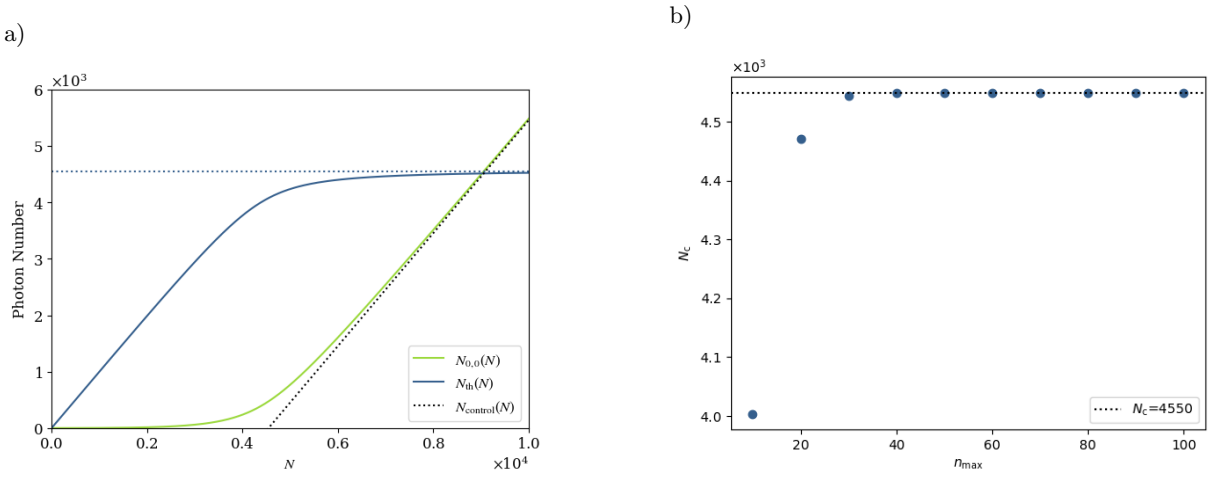


Fig. 3.5: **a)** Ground- and thermal-state particles plotted against the total particle number within the system. The dotted blue line at N_c serves as a reference to show the convergence of N_{th}. Values for both graphs are taken from Fig. 3.4. **b)** Convergence of the critical particle number dependent on highest considered quantum number in x- and y-direction.

from the graph of the thermal particles by looking at the intersection of $N_{0,0}$ and N_{th}. In approximation, consider a system not regarding spontaneous emission. Here the equations

$$N_{0,0}(N) = \Theta(N - N_c)[N - N_c]\,, \tag{3.29}$$

$$N_{th}(N) = N - N_{0,0} = N - \Theta(N - N_c)[N - N_c] \tag{3.30}$$

where Θ is the Heaviside function [13], describe the particle behavior. This means that for

$$N_{th}(N') = N_{0,0}(N')\,, \tag{3.31}$$

simply $N' = 2N_c$ results. Since spontaneous emission has no effect on the critical particle number of a system, it can be checked whether this relation is fulfilled for Fig. 3.5a). This procedure yields $N_c^{th} \approx 4530$ in agreement with N_c derived from the ground-state particles. Now as L is the only freely tunable parameter for the closed system, the behavior of particle occupation for different box lengths can be compared. This also opens up the possibility of numerically addressing errors in measurement in regards to the size of the box length which are approximately $\pm 1\,\mu m$ [6]. As $E \propto 1/L^2$, measurement for large L becomes increasingly difficult as the ground-state energy approaches the floor-noise potential [6] making a discernment between the two nigh impossible. Due to this for the following numerics only box sizes up to $60\,\mu m$ are discussed due to experimental relevance. As finding solutions to the rate equations is substantially more time consuming than summation over a BE-distribution, it would be best to choose a smaller box for the open-dissipative numerics, as for smaller lengths it is expected that the number of modes needed for the critical particle number to converge is less. To this end, first it is needed to be shown that for different L the behavior of $N_{0,0}$ and N_{th} stays the same among each box.
Within Fig. 3.6 this is shown, as for the depicted $L = \{10, 20, 30, 40, 50, 60\}\,\mu m$ the behavior for large N in regards to $N_{0,0}$ and N_{th} stays the same, only differing in the amount of particles needed for condensation to set in. Here also a proper distinction to the harmonic system can be seen. Looking at either the plots for ground or thermal particles, the gaps between them are not equidistant unlike the harmonic trap. This is due to the influence of quantum numbers on the energies within the system. For the box it is $E \propto |\vec{n}|^2$ and for the harmonic trap $E \propto n$ [13]. This is also seen in Fig. 3.7 where a non-linear increase of N_c can be seen for larger box sizes. In order to allow for easier comparison between experiment and numerics, the grey area under and above each points denotes the area in which a measurement for N_c should end up when respecting the error of $\pm 1\,\mu m$ for any L. However as closed system periodic boundary conditions are far removed from the actual set-up, measurements do not lie within this area when simply only accounting for error in lengths. To address this, within [6], further adjustments to the numerics

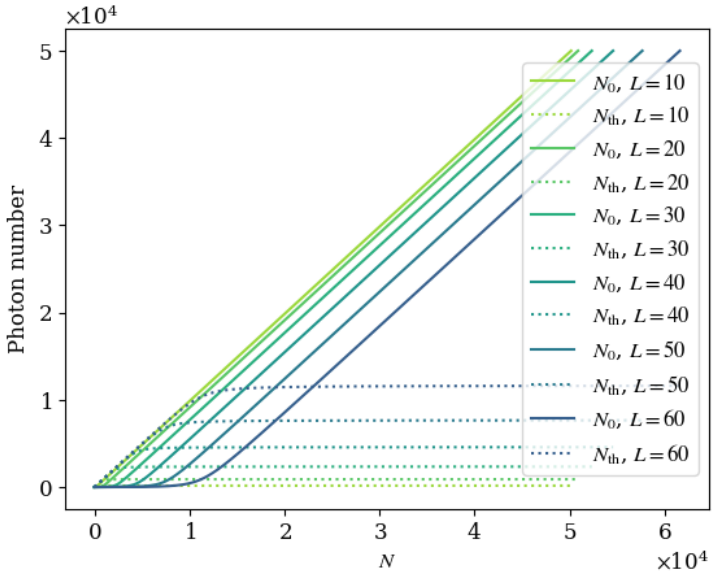


Fig. 3.6: Thermal and ground-state particles plotted against N for varying L considering periodic boundary conditions.

were made by discarding all modes with higher energy than the trap depth of $1.4\,k_\mathrm{B}T$. As the quantum mechanics for a finite trap however fundamentally change the underlying system and its wave equation, also partially letting the photon wave-equation enter the box walls, this idea shall here be disregarded as such a comparison could be made under wrong assumptions. Following this, now consider n_max for the different box lengths as given in Tab. 1. This makes $L = 20\,\mu\mathrm{m}$ an opportune length to use for later

Table 1: Largest needed n_x, n_y for convergence of N_c for different L.

L [μm]	10	20	30	40	50
N_c	161	891	2331	4550	7592
n_max	20	30	40	50	60

numerics, as it needs few modes for convergence yet has a high enough critical particle number so that differences in N_c due to parameter changes are not lost within numeric inaccuracy. This, of course, needs to be verified later on again, however it gives a proper starting block upon which to build. The n_max here do not necessarily give insight for the ones using dirichlet boundary conditions as the summation is vastly different. For this section, c_0 as in (3.17) will not be examined for the calculated systems. However as proof of concept, to partially verify the analytical solution it can be checked whether it predicts the behavior of the critical particle number for growing L. For this, revisit (3.12). The critical particle number

$$N_\mathrm{c} = -\frac{L^2}{\lambda_\mathrm{th}^2}\ln\left(1 - e^{-\frac{\lambda_\mathrm{th}^2}{L^2}c_0}\right) \tag{3.32}$$

can be approximated in first order for $(\lambda_\mathrm{th}^2/L^2)\cdot c_0 \ll 1$ as $N_\mathrm{c} \approx -\frac{L^2}{\lambda_\mathrm{th}^2}\ln(1-(1-\frac{\lambda_\mathrm{th}^2}{L^2}c_0))$ yielding

$$N_\mathrm{c} = \frac{L^2}{\lambda_\mathrm{th}^2}\ln\left(\frac{L}{\lambda_\mathrm{th}}\right) \tag{3.33}$$

for the critical particle number. Note that the influence of c_0 is negligible for the scaling as $c_0 \ll \ln(L^2/\lambda_\mathrm{th}^2)$ holds for large L. This behavior is seen within Fig. 3.7, confirming that the underlying form of the analytical solution and the prior made assumption is correct at least for the considered box lengths.

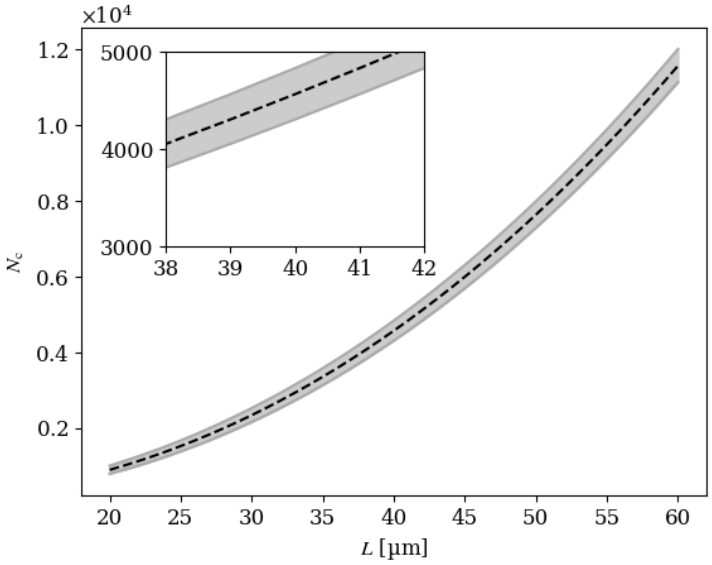


Fig. 3.7: Depicted in dashed black is the critical particle number plotted against the box length for periodic boundary conditions. The gray area around the line denotes where potential measurements would be expected for a given box length. The inset serves the purpose of better showing the order of magnitude of the error.

3.2.2 Dirichlet boundary conditions

Moving one step closer to the experimental conditions, now Dirichlet boundary conditions are considered. Again, starting off the energy eigenvalues (2.19) are introduced to the Bose-Einstein distribution (2.50)

$$\sum_{n_x,n_y=1}^{\infty} N_{n_x,n_y} = \sum_{n_x,n_y=1}^{\infty} \frac{1}{e^{\frac{\pi^2\hbar^2}{2Mk_\mathrm{B}TL^2}(n_x^2+n_y^2)-\frac{\mu}{k_\mathrm{B}T}}-1} \tag{3.34}$$

where when expressing the energy in terms of the thermal wavelength

$$E_{n_x,n_y} = \frac{\pi^2\hbar^2}{2Mk_\mathrm{B}TL^2}(n_x^2+n_y^2) = \frac{\pi}{4}\frac{\lambda_\mathrm{th}^2}{L^2}(n_x^2+n_y^2) \tag{3.35}$$

the expression

$$\sum_{n_x,n_y=1}^{\infty} N_{n_x,n_y} = \sum_{n_x,n_y=1}^{\infty} \frac{1}{e^{\frac{\pi}{4}\frac{\lambda_\mathrm{th}^2}{L^2}(n_x^2+n_y^2)-\frac{\mu}{k_\mathrm{B}T}}-1} \tag{3.36}$$

is garnered. Naturally as the only difference is between a factor two in the k-vectors, the energy seen in 2.26 and 2.19 differs only by the summation and a factor of four. Overall, this section will be similar in all points to that of the periodic boundary conditions however more in depth at necessary points. Starting off again with the behavior of $N(\mu)$, the cavity cut-off energy is again absorbed into the chemical potential to form $\tilde{\mu}$. However as the ground-state energy is not $E_\mathrm{cut}+0$ as for periodic boundary conditions, now it is

$$E_\mathrm{g} = E_\mathrm{cut} + E_{1,1} = E_\mathrm{cut} + \frac{\pi}{2}\frac{\lambda_\mathrm{th}^2}{L^2}. \tag{3.37}$$

Thus the ground-state particles get an additional term in the exponent

$$N_{1,1} = \frac{1}{e^{\beta(\frac{1}{\beta}\frac{\pi}{2}\frac{\lambda_\mathrm{th}^2}{L^2}-\tilde{\mu})}-1}, \tag{3.38}$$

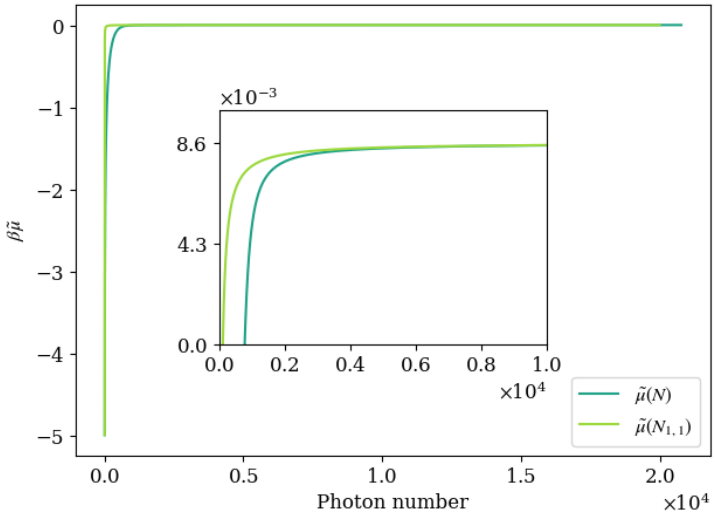


Fig. 3.8: Shown is $\tilde{\mu}$ both for the ground-state and overall particle number. As both curves largely overlap, the inset serves to depict the difference of both close to the ground-state energy level.

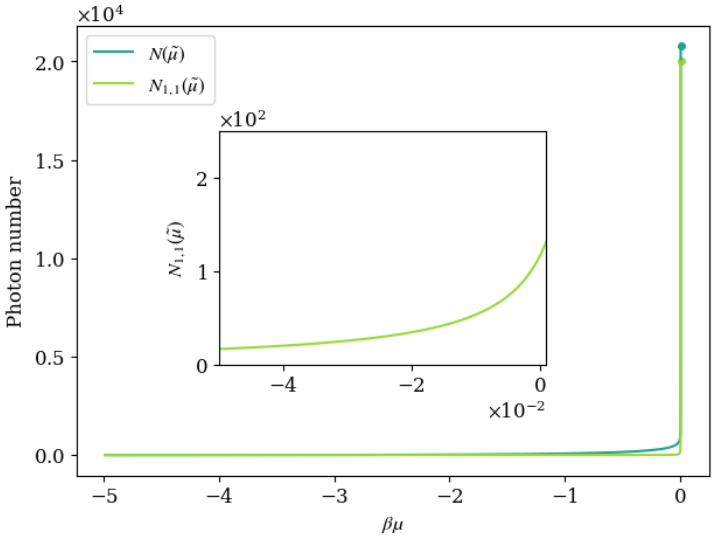


Fig. 3.9: Graph of the equation of state $N(\tilde{\mu})$ for ground-state and overall particle number.

so that now $\tilde{\mu} \to E_{1,1} = \frac{1}{\beta}\frac{\pi}{2}\frac{\lambda_{\mathrm{th}}^2}{L^2}$ $(N \to \infty)$ follows for the shifted chemical potential. As an example, for a box of the length $L = 20\,\mu\mathrm{m}$ the shifted ground-state energy is $E_{1,1} = 0.22\,\mu\mathrm{eV}$. For the plots scaled with β, this means $\beta\tilde{\mu} \to 8.602 \cdot 10^{-3}$ $(N \to \infty)$. This is shown to be accurate within the inset of Fig. 3.8, which also depicts the chemical potential of the ground-state particles converging towards the same value. Now changing the axis to gain again the graph depicting the equation of state $N(\tilde{\mu})$, these graphs can be used to gain, as explained earlier in the periodic section, the sought after curves $N_{\mathrm{th}}(N)$ and $N_{1,1}(N)$. Comparing Fig. 3.4, Fig. 3.8 and Fig. 3.9 it can already be seen, that the Dirichlet boundary conditions overall yield less particles within the system. This becomes apparent when comparing both sets of endpoints for the graphs depicting photon number dependent on $\beta\tilde{\mu}$ as the closer they are, the lower the number of thermal particles. First, as the two prior graphs were constructed for $L = 20\,\mu\mathrm{m}$, the critical particle number resulting is $N_{\mathrm{c}} = 778$ as depicted in Fig. 3.10. Furthermore, (3.29) and (3.30) are also shown as graphs. Note that $N' = 2N_{\mathrm{c}}$ here also seemingly acts as a good approximation, growing in accuracy for larger L as seen in Fig. 3.11. For the thermodynamic limit it can be expected that the graphs follow along more closely to the Heaviside functions.

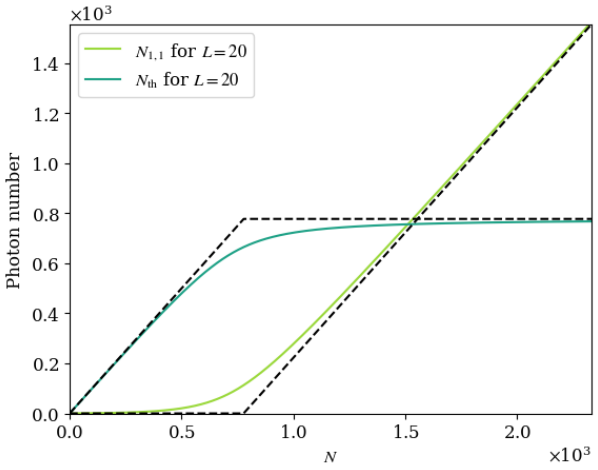


Fig. 3.10: Ground-state and thermal particles $N_{1,1}$ and N_{th} plotted against N using Dirichlet boundary conditions for $L = 20\,\mu\mathrm{m}$. The dashed black lines denote Heaviside functions akin to (3.30). The initially linear growing and then saturated Heaviside function is that of the thermal particles while the other is that of the ground-state ones.

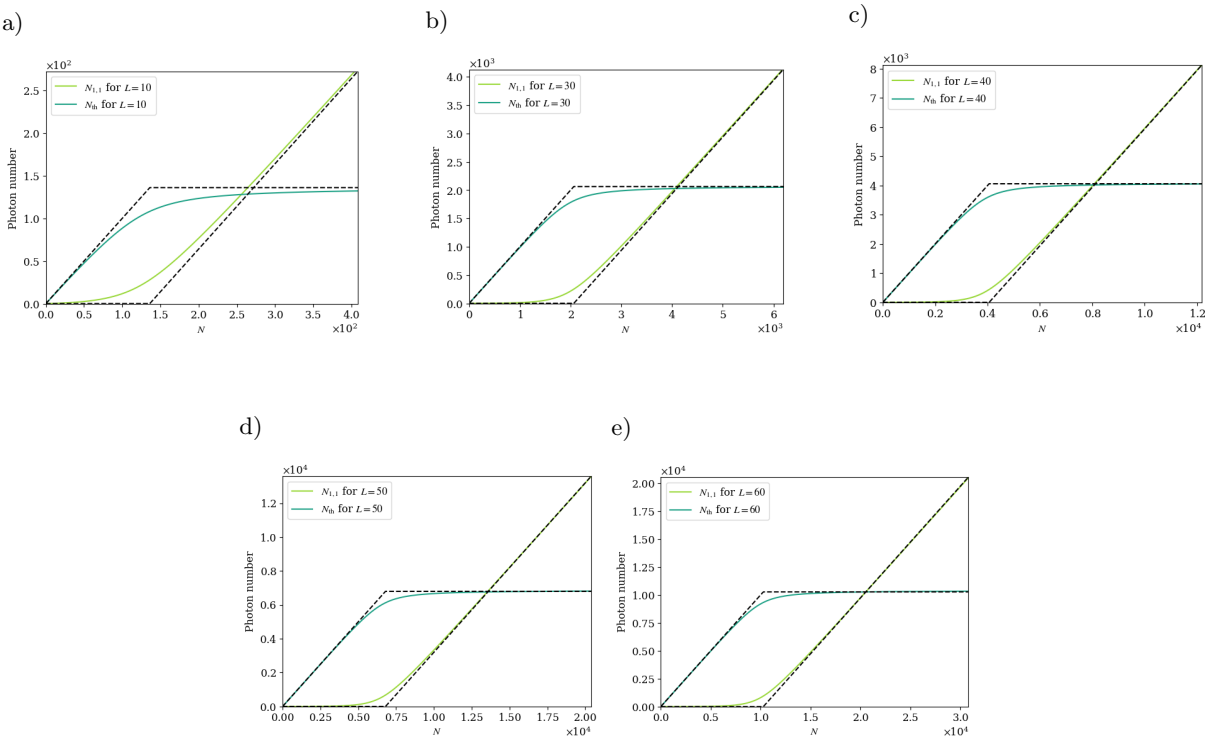


Fig. 3.11: Ground-state and thermal particles $N_{1,1}$ and N_{th} plotted against N for **a)** $L = 10\,\mu\mathrm{m}$ **b)** $L = 30\,\mu\mathrm{m}$ **c)** $L = 40\,\mu\mathrm{m}$ **d)** $L = 50\,\mu\mathrm{m}$ **e)** $L = 60\,\mu\mathrm{m}$. The dashed black lines are explained in Fig. 3.10.

In order to observe this, multiple plots for the thermal and ground-state particles are given in Fig. 3.11 along with their respective Heaviside functions. The critical particle number for Dirichlet boundary conditions and $L = 40\,\mu\mathrm{m}$ is $N_{\mathrm{c}} = 4060$ as shown in Fig. 3.11c), roughly 500 photons less than calculated for the periodic system. As the error of measuring photons is in the realm of 10%, this would not be experimentally discernable [2]. Thus for this length there is not necessarily a sufficient difference in the critical particle number to see the difference of both boundary conditions. It is shown, that for small

and large particle numbers, the Heaviside functions act as a near perfect fit, especially as L grows larger. Near the point of criticality however, the graphs deviate from this behavior and the distance between them increases. Finite-size corrections akin to the IR cut-off scalar c_0, or the fact that for a lower number of overall photons spontaneous emission plays a larger role, can both explain the discrepancy and why it shrinks for $L \to \infty$. Another observation is, that for $L \geq 50\,\mu\text{m}$ the thermal particles seem to saturate slightly above the Heaviside function, which leads to assume that as all graphs have sufficient modes to ensure convergence, for larger L a problem arises with determining N_c. Yet as the error, is so small (order $\sim 10^1$), there would be no way to measure it currently.

3.3 Calculations for IR cut-off

To avoid confusion, the analytical solution will be denoted with an extra top script 'ana' in this subsection. Now equipped with the knowledge of how to numerically calculate the critical particle number for the closed system for different lengths and boundary conditions, (3.12) and (3.17) can be analyzed further. Within Fig. 3.12 the thermal particles for six different box lengths are plotted together with their respective analytical solutions. To this end, for every box length N_c was determined numerically. Following this, c_0 was calculated using (3.17), after which $N_\text{th}^\text{ana}(\mu)$ was plotted based on (3.12). For the periodic boundary conditions this can then be plotted against the numerically calculated $N(\mu)$ giving $N_\text{th}^\text{ana}(N)$ which is seen in Fig. 3.12a). As the analytical solution is derived using periodic boundary conditions the chemical potential has to be adjusted when calculating it for Dirichlet boundary conditions. This results in the equation

$$N_\text{th}^\text{ana}(\tilde{\mu}) = -\frac{L^2}{\lambda^2}\ln\left(1 - e^{\frac{\tilde{\mu}-E_{1,1}}{k_\text{B}T}-\frac{\lambda^2}{L^2}c_0}\right) \tag{3.39}$$

where $\tilde{\mu}$ is the shifted chemical potential for dirichlet boundary conditions as defined in the prior section. Considering this, again $N_\text{th}^\text{ana}(N)$ can be plotted as seen in Fig. 3.12b). Since N_c depends on L, in return this explains c_0 depending on L which is seen in both sub figures. For the used lengths, the c_0 determined through periodic boundary conditions is always smaller than that for Dirichlet boundary conditions. Added to that, c_0 increases more steeply for the Dirichlet case. Interestingly, even though the dirichlet boundary conditions lead to a different integral due to differences in summation and have a differing expression for the energy, the analytical solution works well in describing the numerics. As the behavior was already proven similar for both systems, this means that the aforementioned problems can be absorbed into c_0. Overall, especially for smaller boxes, the analytical solution is a good approximation of the numerics. For larger L, slight differences can be made out, which is due to the finding mentioned in the prior section, that for increasing box lengths, the critical particle number determined from the ground-state particles differs slightly from that of the thermal particles. Lastly, Fig. 3.12 indicates, especially for smaller L, that c_0 is independent of N. Since N is dependent on μ, this also means that c_0 is independent of μ. As predicted, within Fig. 3.13 it can be seen that the ratio $\frac{c_0}{L^2}$ of the IR cut off and two-dimensional box area vanishes for larger L for both boundary conditions. This result is consistent with the thermodynamic limit, as there differences between periodic and Dirichlet boundary conditions disappear. On the contrary, for small L the ratio diverges clearly showing the impact of finite-size corrections within the systems. Put together these results indicate for the examined box lengths, that (3.12) is a good approximation of the numerical behavior calculated for the system. It is to be noted however, that as of now there is no equation to calculated c_0 independently of a measurement or numerical approximation of the critical particle number. Only after this is achieved, can the analytical solution be properly used.

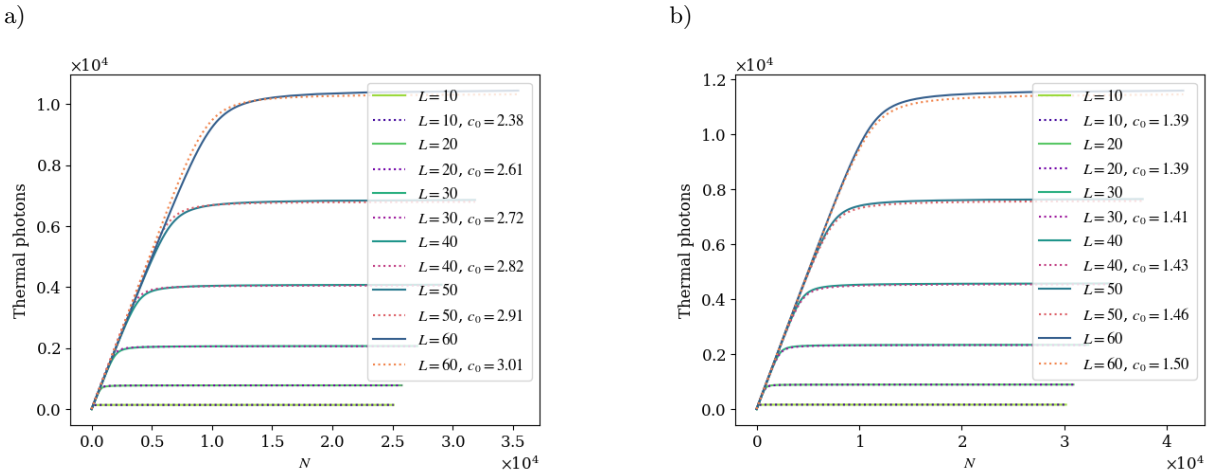


Fig. 3.12: Comparison of analytical solution to closed system numerics for **a)** Dirichlet boundary conditions and **b)** periodic boundary conditions. The solid lines indicate numerical results for thermal occupation, whereas the dotted lines are the thermal particles calculated using (3.12).

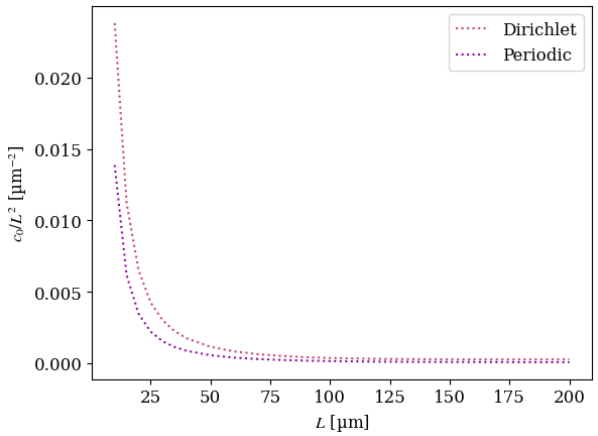


Fig. 3.13: Comparison of scalar c_0 for the IR cut-off k_0 for different L considering Dirichlet and periodic boundary conditions.

4 Open dissipative system

Within this section the open-dissipative nature of the system is analyzed. To this end, convergence conditions are examined and different influences upon the system due to non-radiative and cavity losses are studied. This results in clear differences to the closed system. The numerics here are done considering dirichlet boundary conditions and a molecule number $M = 10^{10}$.

4.1 Open dissipative approach

Dealing with the open dissipative nature of a system complicates the numerics by a large margin. The particle distribution now changes to

$$N_{n_x,n_y} = \frac{1}{e^{\beta(E_{n_x,n_y}-\mu)} - 1 + \frac{\Gamma_c(E_{n_x,n_y})}{B_{21}(E_{n_x,n_y})M_2}} \tag{4.1}$$

and the approach for the closed system numerics can no longer be used, as a set of rate equations (2.56), (2.57), (2.58) is now required as derived earlier. This results in one equation for the excited dye molecules, one for the ground state dye molecules and for $n_x^{\max} = n_y^{\max} = n$ in n^2 equations for the photon modes where 'max' denotes the largest quantum number in each direction. Thus overall $n^2 + 2$ equations which need to be solved iteratively numerically. Using the results from the closed system, to be deeply withing the converged realm roughly $n_x^{\max} = n_y^{\max} = 100$ is needed, meaning 10,000 modes and 10,002 equations have to be calculated. To reduce the number of equations and computation time needed, it is appropriate to use the symmetry of the energy levels i.e. $E(a,b) = E(b,a)$, and introduce an effective photon mode n_{eff} as it is expected that the particles of a given energy level e.g. $E(1,2) = E(2,1)$ are distributed evenly between the degeneracies of the mode. For the given example, this means that half of the photons are in the $E(1,2)$ and the other half in the $E(2,1)$ mode. This approach requires the knowledge over which modes exist and what their degeneracies are. This is realized through an intuitive approach, by creating a matrix $A = (a_{ij})_{ij}\,,\ i,j \in \mathbb{N}$ with the elements $a_{ij} = i^2 + j^2$ and counting its unique entries (n_{eff}) and the amount of times they exist within the matrix (degeneracy $g(n_{\text{eff}})$ of the effective mode). For $n_x^{\max} = n_y^{\max} = n = 3$ this results in the matrix $A^* = \begin{bmatrix} 2 & 5 & 10 \\ 5 & 8 & 13 \\ 10 & 13 & 18 \end{bmatrix}$ and the values $n_{\text{eff}} \in \{2,5,8,10,13,18\}$ with the respective degeneracies $g(n_{\text{eff}}) = \{g(2) = 1, g(5) = 2, \dots\}$.
Instead of the original 10,000 photon mode equations, this approach just leaves a little more than a third of that with 3605 unique modes. The number of photons $N_{n_{\text{eff}}}$ for each n_{eff} is calculated in steady state using (2.64), (2.65) and (2.58) and then multiplied with the degeneracy of the mode $N = N_{n_{\text{eff}}} \cdot g(n_{\text{eff}})$ to gain the total particle number

$$N = \sum_{n_x=1}^{n_x^{\max}} \sum_{n_y=1}^{n_y^{\max}} N(n_x,n_y) = \sum_{n_{\text{eff}}} \frac{g_{\text{eff}}}{e^{\beta(E_{n_{\text{eff}}}-\mu)} - + \frac{\Gamma_c(E_{n_{\text{eff}}})}{B_{21}(E_{n_{\text{eff}}})M_2}}. \tag{4.2}$$

4.2 Analytical fit of Einstein coefficients and cavity losses

For properly calculating the open-dissipative case, it is imperative to know the Einstein coefficients $B_{21}(E_{n_{\text{eff}}})$ and $B_{12}(E_{n_{\text{eff}}})$ for any given energy. To this end, as Rhodamine 6G is considered for a dye solution, the high-precision experimental data [17] for its absorption and emission spectrum is used to model the coefficients. As measurements only have a finite spacing, more numerical approaches need to be employed. Desired as a result are two fitting functions, one for $B_{21}(E_{n_{\text{eff}}})$ and one for $B_{12}(E_{n_{\text{eff}}})$. In this respect it is helpful that in the theory section the Kennard-Stepanov relation (2.49) was already derived, which gives a relationship between the two. In theory, this means that only for one of the two a fit has to be found, while the other can then be expressed simply by multiplying the former with an exponential function. To model the experimental data, a summation of Gaußcurves

$$B_{21}(E) = \sum_{i=1}^{n} A_i e^{-\frac{(E-\theta_i)^2}{2\sigma_i^2}} \tag{4.3}$$

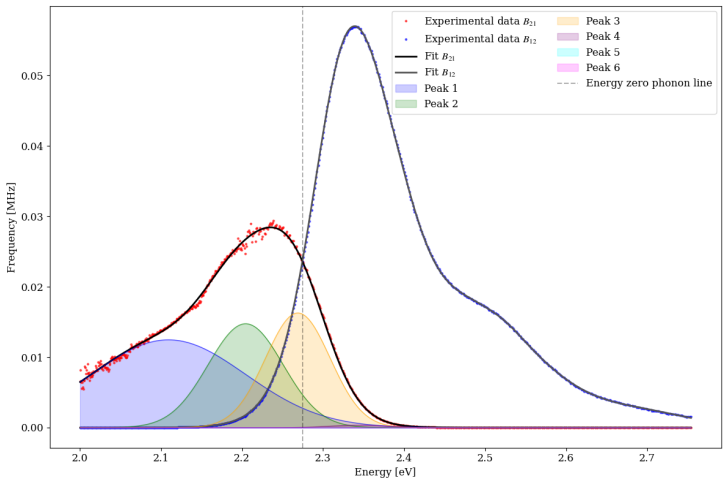


Fig. 4.1: Einstein coefficients of absorption ($B_{12}(E)$) and stimulated emission ($B_{21}(E)$) plotted against photon energy E using experimental data. All data was measured for the TEM_7 mode [17] seen in Fig. 2.4.

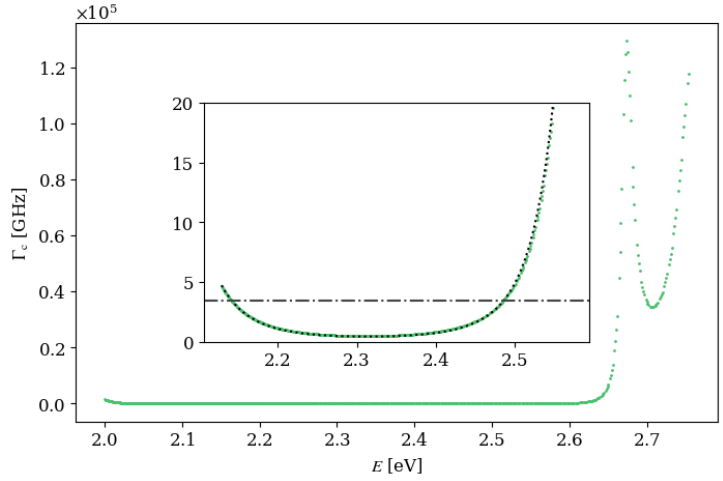


Fig. 4.2: Cavity losses $\Gamma_\mathrm{c}(E)$ plotted against photon energy E seen in green. Black dotted-line indicates a fitting function calculated using (4.5). All data was measured for the TEM_7 mode [17] seen in Fig. 2.4.

was used, where σ denotes the standard deviation. To avoid confusion with the chemical potential, here the expectation value is given as θ instead of the commonly used μ. For the numerics it turns out that six peaks are sufficient to model both coefficients. The finalized fits can be seen in Fig. 4.1. Each of the shaded areas denotes a distinct Gauß curve used to fit B_{21}. Individual peak positions can be interpreted as the energy of a vibrational state [13]. Furthermore, the energy of the zero phonon line $E_\mathrm{ZPL} \approx 2.275\,\mathrm{eV}$ is depicted in dashed grey. From the rate equations, it is apparent that having a fit to determine the absorption and emission coefficients at any time is not yet enough, as the cavity losses Γ_c are also energy dependent. This can be addressed in two separate ways, the first being a fit of the cavity losses as a function of the photon-mode energy and the second being an average of the losses calculated for the given system. The chosen approach is to consider an average Γ_c which can be calculated via the following integral [13]

$$\Gamma_\mathrm{c} = \frac{1}{E_\mathrm{max} - E_\mathrm{cut}} \int_{E_\mathrm{cut}}^{E_\mathrm{max}} \mathrm{d}E\, \Gamma_\mathrm{c}^\mathrm{fit}(E) \tag{4.4}$$

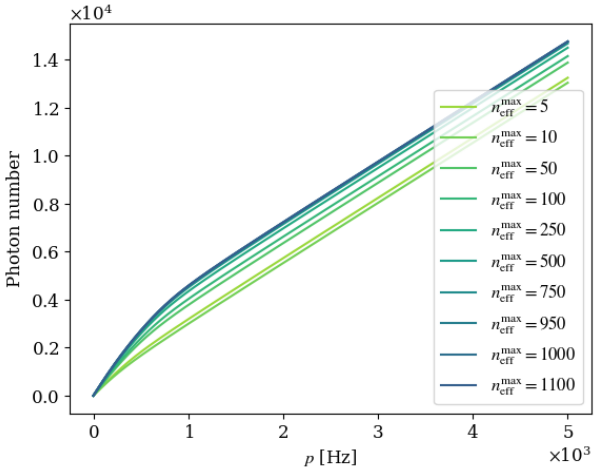


Fig. 4.3: Total cavity photons depending on pumping rate p for $L = 40\,\mu\text{m}$ and $\Gamma_c = 4.00\,\text{GHz}$.

where

$$\Gamma_c^{\text{fit}}(E) = e^{a(E-b)^2+c} \tag{4.5}$$

denotes a fitting function where a, b and c are fitting parameters. This averages the cavity losses over a maximal and minimal (cut-off) energy considered. The fit as well as the experimental data can be seen in Fig. 4.2. For the given data [17] this comes out to a cavity loss rate of about $\Gamma_c \approx 3.5\,\text{GHz}$ as seen in the inset of Fig. 4.2, which is close to the loss rate $\Gamma_c \approx 3.33\,\text{GHz}$ for a box cavity given here as an example [6]. Note that the cavity losses gained through the fit can vary slightly when considering different energy intervals. As the cavity losses do not influence the absorption and emission coefficients, Γ_c can also be left as a freely tunable parameter for the following sections.

4.3 Numerical convergence

First it needs to be determined at which point the numerical simulation has converged. Thus an $n_{\text{eff}}^{\text{max}}$ needs to be calculated for which when increasing it, no further or very little change in the particle number is seen. To this end two different lengths $L = 20\,\mu\text{m}$ and $L = 40\,\mu\text{m}$ are analyzed. The former box was chosen due to the closed system numerics, with the latter serving as a comparison. This ultimately shows the vast difference in computation time between smaller and larger boxes, as more and more modes need to be considered due to the dependence $E \propto 1/L^2$. For this section, as only interest lies within numerical convergence and the critical particle number, $\Gamma_{\text{nr}} = 0$ is considered and if not stated differently, $\Gamma_c = 4.00\,\text{GHz}$ was used. With the cut-off energy $E_{\text{cut}} \approx 2.073\,\text{eV}$ [6, 17] now the rate-equations can be solved giving the total particle number within the system depending on the external pumping rate p. This yields a direct connection between the number of photons within the cavity, and a tunable and measurable experimental parameter as seen in Fig. 4.3. The non-regular distances between the considered maximum modes is chosen deliberately, as it shows that for a difference of five modes between $n_{\text{eff}}^{\text{max}} = 5$ and $n_{\text{eff}}^{\text{max}} = 10$ there is a noticeable difference in particles, whereas for a difference of 600 modes between $n_{\text{eff}}^{\text{max}} = 500$ and $n_{\text{eff}}^{\text{max}} = 1100$, no apparent change can be made out in this graph. These graphs also allow for considering a different parameter to indicate criticality of the system, namely the critical pumping rate p_c. For now it is not determined, however consider each graph ends parallel to one another after a certain pumping rate. This indicates that after a specific pumping rate depending on $n_{\text{eff}}^{\text{max}}$ for the given system is reached, the thermal states are fully occupied and the system then grows linearly with the pumping rate. This observation is supported by the rate equations, as when considering only a single mode, the ground state, then (2.65) yields

$$0 = pM_1 - \Gamma_{\text{nr}} M_2 + N_{1,1}\Gamma_c \tag{4.6}$$

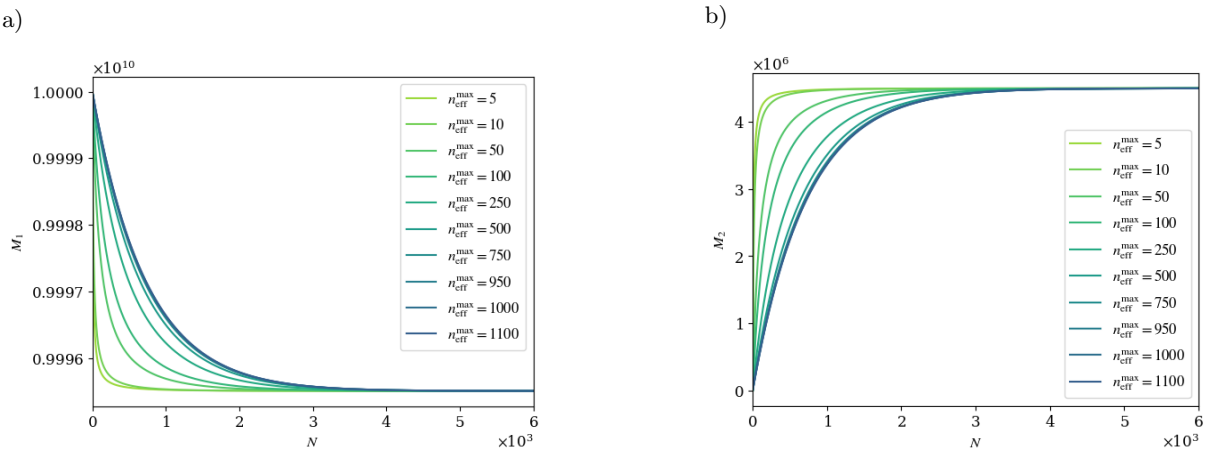


Fig. 4.4: Molecular occupation for **a)** ground-state molecules and **b)** excited molecules. Considered is $L = 40\,\mu\text{m}$.

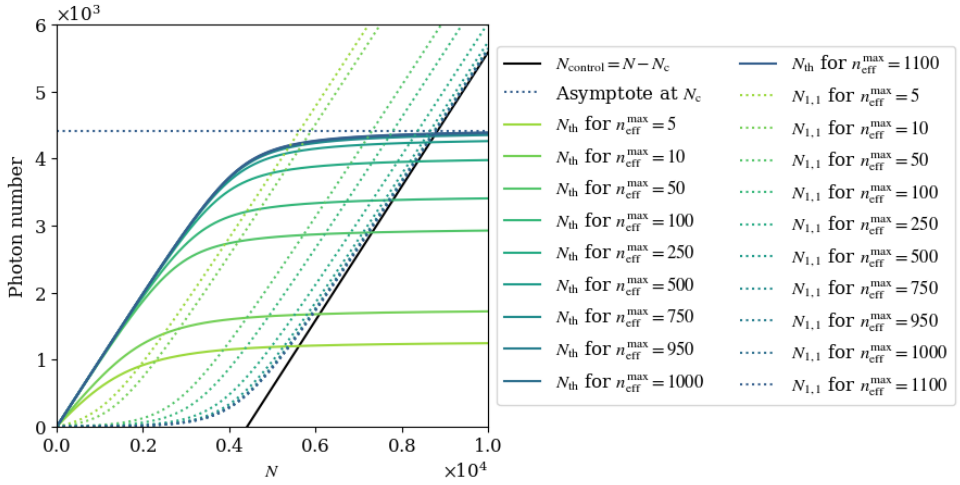


Fig. 4.5: Solutions of the rate equations for different considered mode counts and $L = 40\,\mu\text{m}$.

when respecting (2.64). Solving for $N_{1,1}$ gives the equation

$$N_{1,1} = \frac{pM_1 - \Gamma_{\text{nr}} M_2}{\Gamma_{\text{c}}} \tag{4.7}$$

which shows a linear increase in p. It may however be argued that, as the molecular occupation depends on p, this does not suffice as evidence for a linear proportionality as $M_1(p)$ and $M_2(p)$ are not yet given. Consider Fig. 4.4 which shows, that for large enough N, both molecule states saturate, yielding

$$\frac{\partial M_1}{\partial p} = \frac{\partial M_2}{\partial p} = 0 \; (N \to \infty). \tag{4.8}$$

This as explained earlier, directly corresponds to the behavior for large p as well. Taking into account that the cavity losses are independent of the pumping strength, the proportionality $N_{1,1} \propto p$ is concluded here. Note that this derivation was done for $\Gamma_{\text{nr}} = \text{const.} > 0$, meaning it stands independent of the fact that this section neglects non-radiative losses as all arguments hold in both cases. Now, when simultaneously solving for $N_{1,1}(p)$ and $N(p)$, one can calculate $N_{\text{th}}(p)$. This again allows to plot both the ground-state and thermal particles against N. Doing this, Fig. 4.5 offers a better resolution of the differences in particle occupation for the different considered modes as more distinctions between the curves can be

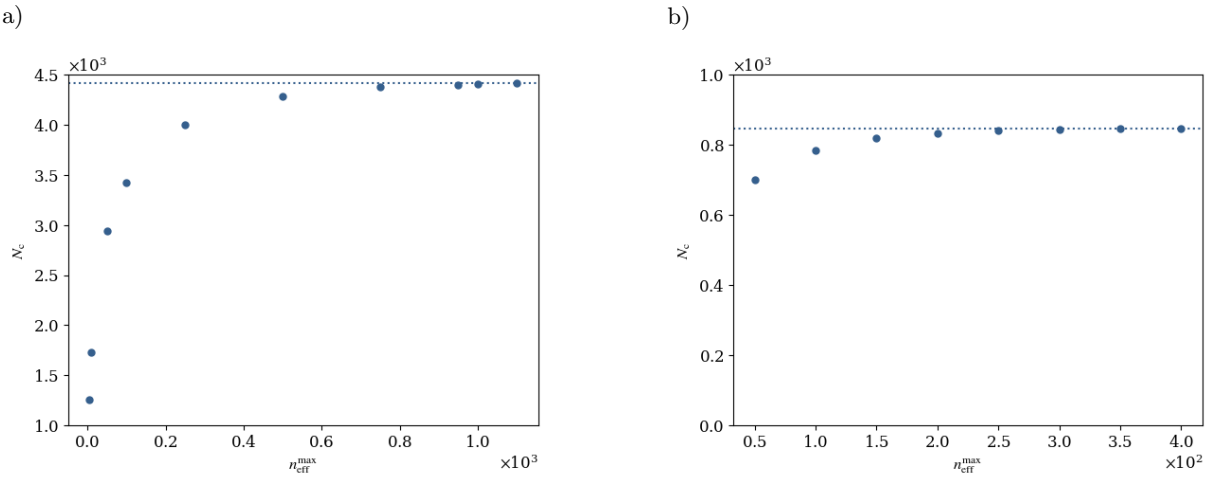


Fig. 4.6: Convergence of the critical particle number N_c dependent on mode count for **a)** $L = 20\,\mu m$ and **b)** $L = 40\,\mu m$.

made. Where as Fig. 4.3 would lead to assume that convergence is reached around 500 modes, here it shows that at least 750 modes have to be taken into account, with presumably even more needed. In both graphs, each curve is shown to change its behavior over a finite area and not a kink like the earlier Heaviside functions. For the p dependent graph such a kink denotes the critical pumping rate and for the N dependent graph the critical particle number. The latter turns out to be $N_c = 4416$ for this parameter set when considering 1100 modes, around 350 photons more than for the closed system when respecting dirichlet boundary conditions as seen in Fig. 3.11c). It may be expected, but this shows that the cavity-losses directly lead to a change in critical particle number. Namely cavity losses increase its value as more photons are needed to saturate the thermal states when particles can vanish. This, similarly to earlier comparisons, also lies within the experimental error bars [2], meaning the effect here cannot be clearly measured. In comparison with the harmonic trap, the kink of each graph is way less pronounced [13], which is simply due to the fact that the expected photon numbers are an order of magnitude smaller for the box than for the harmonic confinement, making the actual roundness of the curve more visible. As in the case for the closed system and the used Heaviside functions, the graphs should approach such a form when neglecting the spontaneous emission within the rate equations. Finally the third and most proper way of testing convergence is looking straight at the critical particle number resulting from every $n_{\mathrm{eff}}^{\mathrm{max}}$ within Fig. 4.6a).
After $n_{\mathrm{eff}}^{\mathrm{max}} = 750$, any change in critical particle for higher considered maximum modes becomes so small, that there is no possibility of ever experimentally verifying it. This means that for $L = 40\,\mu m$, taking into account 950 modes is well within the converged realm. This also means that the increase in calculation time is significant. Note that this is to be considered against the backdrop that within the used code, most likely multiple optimization can still be made to decrease computation time. For now this serves as a clear incentive to consider smaller cavity lengths, as any reduction in needed modes reduces the computation time. Now consider a box length of $L = 20\,\mu m$.
The resulting numerical calculations are shown within Fig. 4.7. As mentioned earlier, Fig. 4.7a) shows that for smaller overall particle numbers, the edge within each graph becomes less pronounced, making it more difficult to identify a critical pumping rate this way. From Fig. 4.7b) a critical particle number $N_c = 847$ can be given for the considered parameters. This was done using $n_{\mathrm{eff}}^{\mathrm{max}} = 400$. This is well within the converged realm as seen in Fig. 4.6b). Considering this, using the $20\,\mu m$ box instead of the $40\,\mu m$ box leads to a reduction in calculation time of up to 90%, whilst not loosing anything from when considering larger boxes. Equivalently to $L = 40\,\mu m$, the critical pumping rate if wanted can simply be gained after using $N_c = N(p_c)$. This means that for every following graph, if not explicitly stated differently, a box length $L = 20\,\mu m$ is considered.

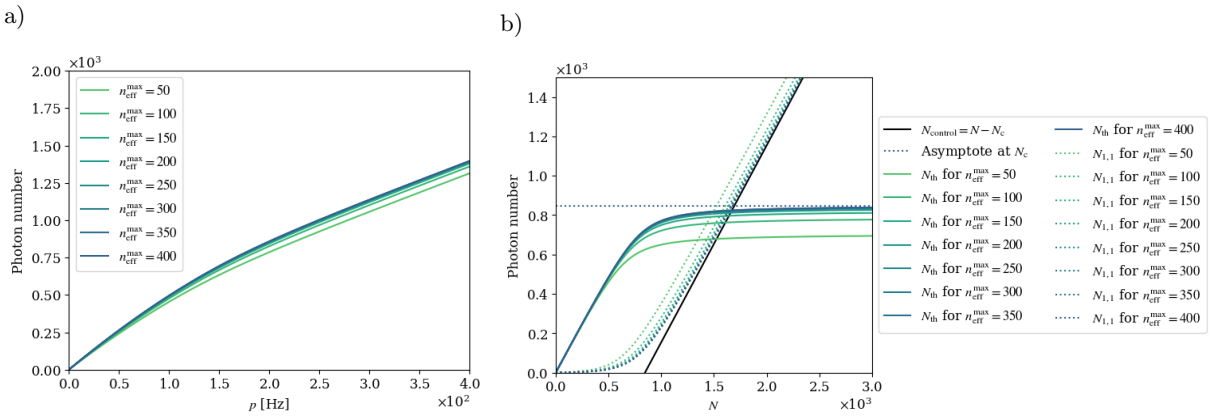


Fig. 4.7: Numerical solutions to the rate equations for $L = 20\,\mu\text{m}$ and $\Gamma_c = 4.00\,\text{GHz}$. **a)** System particle number dependent on external pumping rate. **b)** Occupation of thermal and ground-state particle levels.

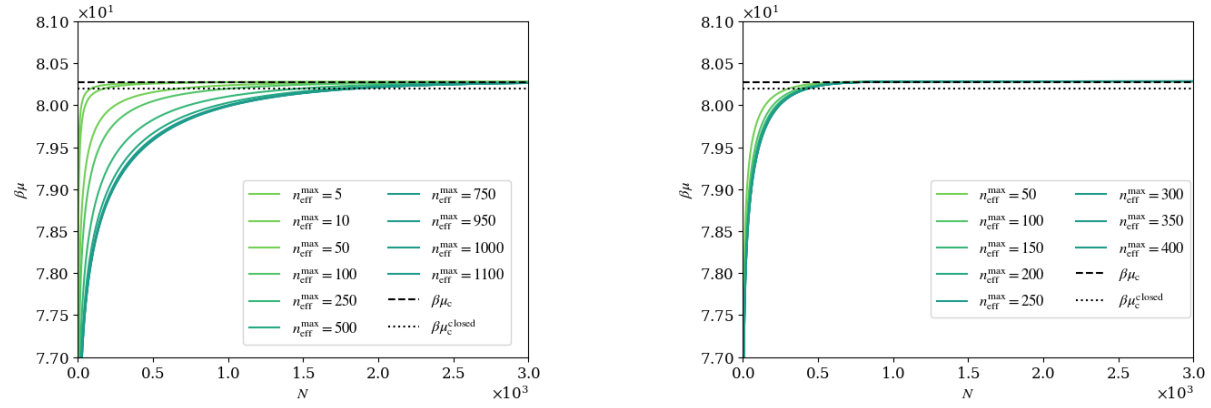


Fig. 4.8: Chemical potential plotted against the system particle number for **a)** $L = 40\,\mu\text{m}$ and **b)** $L = 20\,\mu\text{m}$. Both graphs were calculated using (2.63).

4.4 Open-dissipative chemical potential

The chemical potential serves as another parameter to compare open and closed system approaches. As more particles are needed for condensation in the former, the critical chemical potential must be larger than that of the closed system. This comparison also serves as an accuracy check of the numerics, whether for smaller Γ_c the open-dissipative critical chemical potential approaches that of the closed system. Tying into the previous section, Fig. 4.8 also underlines that a smaller box needs less modes for convergence. The critical chemical potentials for the open system are $\beta\mu_c = 80.2773$ for $L = 40\,\mu\text{m}$ and $\beta\mu_c = 80.2768$ for $L = 40\,\mu\text{m}$. The difference in $\beta\mu_c$ for both systems is so small, that either the critical chemical potential changes in a negligibly small way for different L, or numerical inaccuracies led to the difference. Overall however, box length does not seem to impact the critical chemical potential on this scale. For the closed system limit at $\Gamma_c = 0$ and $\Gamma_{nr} = 0$, $\beta\mu_c^{closed} = 80.1994$ is calculated for both systems using

$$\beta\mu_c^{closed} = \beta E_{cut} \tag{4.9}$$

respecting the condition $\mu \to E_{cut}$ ($\Gamma_c \to 0$) [13]. Note here that unlike in the closed system numerical section, this section deals with the physical, non-shifted chemical potential of the photons. The critical chemical potential in the closed system limit being the same for both boxes means as mentioned, that $\beta\mu_c$ does not depend on the box size. Overall it can be stated, that whilst the cavity losses have a significant

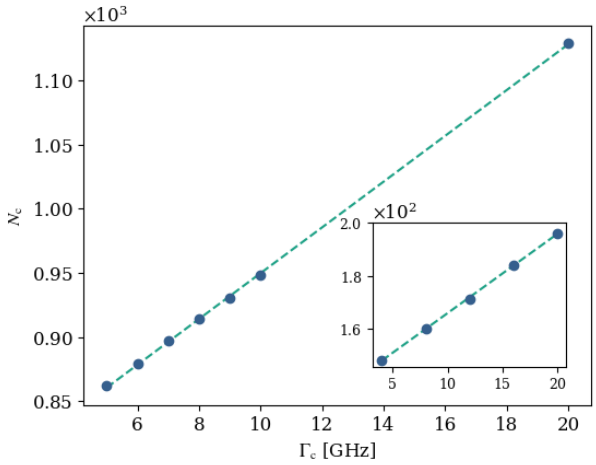


Fig. 4.9: Critical particle number determined for different cavity losses considering a box length of $L = 20\,\mu\text{m}$. The inset depicts the same for $L = 10\,\mu\text{m}$.

effect on the critical particle number as can be seen in the prior section for the two different box sizes, they only negligibly effect the critical chemical potential.

4.5 Influence of cavity losses on critical particle number

Numerically simulating the system for different Γ_c is of interest, as especially for larger considered $n_{\text{eff}}^{\text{max}}$ the influence on the critical particle number is not inherently apparent from the rate equations. Furthermore, it also offers a check for consistency of the numerics. This is due to the condition that for $\Gamma_c \to 0$, the critical particle number of the open system should converge to that of the closed system. Within Fig. 4.9, the blue dashed line was created using a linear fit $N_c = a\Gamma_c - b$ where a with $[a] = \text{s}$ and b are fit-parameters. This method of fitting was chosen after observing the numerical results. The slope of the fit is given by $a \approx 17.83\,\text{s}$. Of special interest is the point at which the linear fit intercepts the N_c-axis. This point is the parameter b and it predicts the closed system critical particle number from the open-system numerics as the limit of N_c for $\Gamma_c \to 0$. The fit result $\lim_{\Gamma_c \to 0} N_c = b \approx 772$ is in very good agreement to the value $N_c = 778$ calculated directly using closed system numerics, which can be seen in Fig. 3.10. This finding expresses that both numerical approaches are consistent with each other, with the closed system being the lower limit of the open-system. Adding to this, the critical particle number for any Γ_c at least up until 20 GHz can be determined once a and b are calculated simply by a linear relation. For any L, b can always be calculated using the closed system as explained earlier. For a different L, namely $L = 10\,\mu\text{m}$, the slope is given by $a \approx 3.00\,\text{s}$. This indicates that a needs to be calculated individually for each system. Whether a connection can be made between the calculated slopes for different systems is a matter for further analysis.

4.6 Non-radiative losses

Lastly, to show whether the made assumption that the non-radiative losses can be neglected for determining the critical particle number and the behavior of the system, different simulations are compared. To this end $\Gamma_c = 5\,\text{GHz}$ and $L = 20\,\mu\text{m}$ are used for every calculation. In Fig. 4.10a) the particle number depending on the pumping rate is depicted for two different Γ_{nr}. Shown is, that different critical pumping strengths result. As the grey dotted line indicates the critical particle number, the first visual proof is given, that the critical particle number does not depend on the non-radiative losses. As the critical particle numbers considered in this thesis are one to two orders of magnitude smaller than those resulting for the harmonic trap, an error arises for this visual approach [13]. Fig. 4.10a) shows, that for an increase in the non-radiative losses, more pumping is needed to reach condensation. This together results in graphs that are overall harder to properly compare for larger Γ_{nr}, as their range grows large quickly. To forego this issue, as the figure shows, the fact that both graphs end up parallel to each other after reaching the

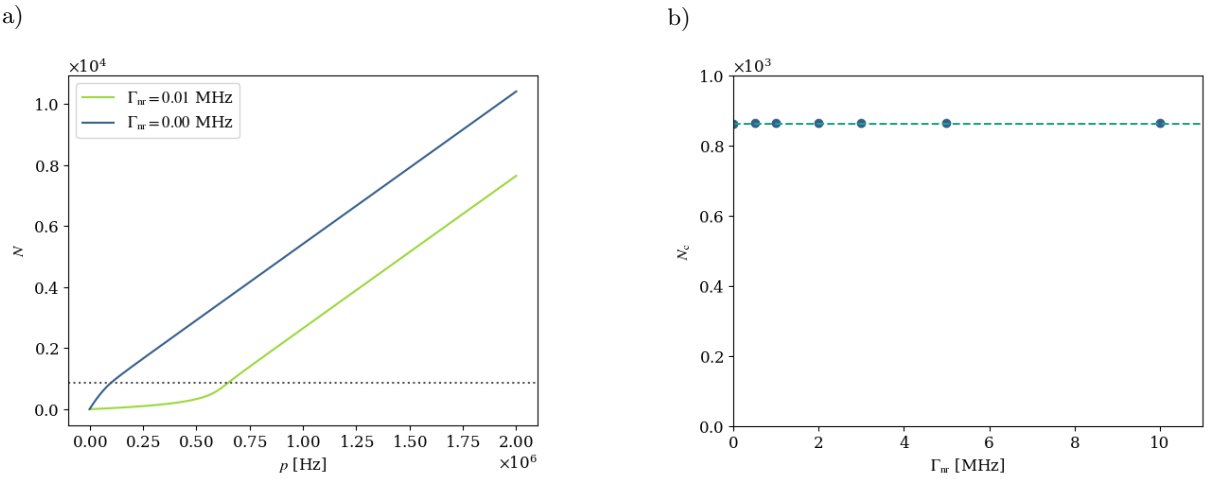


Fig. 4.10: Depicted is the behavior of the system for varying non-radiative losses in regards to **a)** the pumping rate and **b)** the critical particle number. The latter is calculated using (3.21).

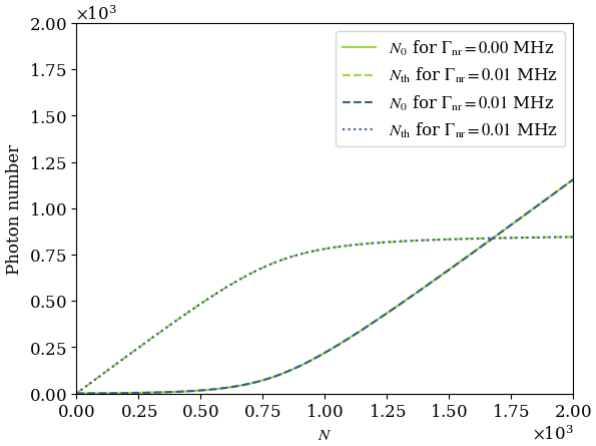


Fig. 4.11: Thermal and ground-state particles dependent on N for different Γ_{nr}.

critical pumping rate can be used. As the same linear behavior is seen, this means that once criticality is reached, the ground-state particles behave in the same way regardless of the non-radiative losses. This means, that if the critical particle number for arbitrary Γ_{nr} is the same, changing it has no influence on the behavior of the system besides a different critical pumping rate. Fig. 4.10b) shows this to be accurate. For the prior numerics, the assumption that the non-radiative losses do not influence the critical particle number is proven to be accurate. To further assert this, Fig. 4.11 depicts that for the given non-radiative losses, the graphs of particle occupation remain the same. As the difference in pumping behavior prior to criticality is already distinct enough for $\Gamma_{\mathrm{nr}} = 0.01\,\mathrm{GHz}$ compared to no non-radiative losses, this is not expected to change for larger Γ_{nr}. This is especially due to the prior observations that the slope of both $N(p)$ graphs as well as their critical particle numbers are the same.

5 Summary and outlook

Ove the course of this thesis, both the closed and open-dissipative system were analyzed intensively. First the description of the experimental set up together with the paraxial approximation (2.2) and the resulting photon dispersion (2.5) was introduced. After deriving the energy eigenstates for a box-trap regarding Dirichlet (2.19) and periodic boundary conditions (2.26), the corresponding quantum statistics were considered. In particular, the Bose-Einstein distribution (2.39) was derived. It was then shown, that one can rederive this exact distribution when considering the heuristically introduced rate equations of the closed system (2.40) and the Kennard-Stepanov relation (2.49). Introducing loss and pump parameters to this approach resulted in a set of rate equations (2.56)-(2.58) for the open-dissipative case. These gave rise to an open-dissipative Bose-Einstein distribution (2.62) which considers an energy independent chemical potential (2.63). Lastly the conditions, which need to be met for Bose-Einstein condensation to occur, were summarized. The description of the closed system started with the derivation of an analytical approximation for the thermal particles N_{th} in (3.12) using periodic boundary conditions. This introduced the concept of an IR cut-off $k_0 = \frac{2\sqrt{\pi}}{L} c_0$ in Eqs. (3.6, 3.11, 3.12). This describes finite-size effects due to the scaling of $k_0 \propto L^{-1}$. Staying with the periodic case, the behavior of the total photon number N depending on a shifted chemical potential $\tilde{\mu}$ was examined within Fig. 3.4. Using this, Fig. 3.5a) illustrates the behavior of ground-state and thermal particle occupation. It was shown, that this happened in the numerically convergent realm within Fig. 3.5b). After this, the ground-state particles N_{g} and N_{th} were calculated for varying lengths, depicted in Fig. 3.6. This allowed for an initial analysis of the critical particle number N_{c} and convergence of the numerics, which is summarized in Tab. 1. Following this, a first examination of the analytical solution was done, which showed using (3.33) in conjunction with Fig. 3.7 that it correctly predicts the scaling of N_{c} for large L. When moving to Dirichlet boundary conditions, Fig. 3.9 together with Fig. 3.10 and Fig. 3.11, showed that a substantial reduction in the critical particle number compared to the periodic case can be seen. Finishing off the closed system, the IR cut-off was further examined, showing within Fig. 3.12 that the analytical approximation matches the numerically predicted curves. In Fig. 3.13, it is confirmed that the ratio $\frac{c_0}{L^2}$ vanishes in the thermodynamic limit, which is the needed behavior confirming that the IR cut-off can be interpreted as a finite-size correction. Moving on to the open system, the numerics now directly depend on the Einstein-coefficients as seen in the rate equations and the simplified total particle number (4.2). To address this, an analytical fit of the coefficients was done using a summation of Gauß curves (4.3) and again the Kennard-Stepanov relation. The result is seen in Fig. 4.1. Following this, the energy dependent cavity losses were approximated as a mean considering (4.4). Using the external pumping rate p, the graphs for $N(p)$ for $\Gamma_{\mathrm{c}} = 4.00\,\mathrm{GHz}$ were calculated for different modes to test convergence seen in Fig. 4.3 for $L = 40\,\mu\mathrm{m}$. Together with Fig. 4.4 and Fig. 4.6a), it was shown that considering a maximum of 950 modes is sufficient to operate in the convergent realm. Within the same section, this was also done for $L = 20\,\mu\mathrm{m}$ in Fig. 4.7 and Fig. 4.6b), showing that here only 400 modes are needed which makes it more practical for following numerics. Respecting cavity losses resulted in a notable difference in critical particle number, i.e. 350 photons for $L = 40\,\mu\mathrm{m}$. Note that this is within the experimental error of about 10% and can not be measured currently. For the two prior mentioned lengths, Fig. 4.8 compares the critical chemical potential when considering the same cavity losses. Shown is that even though there is a noticeable difference in critical particle number, influence on the critical chemical potential is only minor. Adding to that, it was calculated that for both box lengths the closed system limit critical chemical potential is identical. It was then shown, that the critical particle number depends linearly on the cavity losses for at least up to $\Gamma_{\mathrm{c}} = 20\,\mathrm{GHz}$ in Fig. 4.9. To this end, a linear fit $N_{\mathrm{c}}(\Gamma_{\mathrm{c}}) = a\Gamma_{\mathrm{c}} + b$ was used, where a denotes the slope of the fit and b as the offset is the critical particle number of the closed system. Lastly, Fig. 4.10 together with Fig. 4.11 shows that the behavior of the system in regards to the particle number is not disturbed by non-radiative losses at least up until $\Gamma_{\mathrm{nr}} = 10\,\mathrm{MHz}$.

Following this thesis, for the closed system further studying of the analytical solution could be of value. To this end, it should be examined whether the value of the IR cut-off can be derived independent of numerics. This could be done if one examines the curve $c_0(L)$ and determines a fit function for it. This would give the chance to recreate it analytically. In addition to that, it also gives more insight on the actual scaling of $\frac{c_0}{L^2}$. For both the closed and open system, corrections to the considered potential can be made. Here, a perfect box potential was used, which is not realistic for the experiment. Also further examinations for the cavity losses can be made, in determining the linear fitting parameters of $N_{\mathrm{c}}(L)$ for

different L. Using this, one could analyze whether it is possible to predict the critical particle number of varying lengths for different Γ_c from only a single set of fitting parameters a and b.

Acknowledgements

First and foremost I would like to thank Priv.-Doz. Dr. Axel Pelster for his supervision. Throughout the entire course of writing this thesis, he supported me however he could.

Special thanks also go to Joshua Krauß and Leon Mixa, with whom I had many productive discussions furthering my knowledge of the topic.

In addition I would also also like to thank my second reviewer Prof. Dr. Georg von Freymann at the Leibniz University of Hannover.

Lastly I want to thank my friends and family who supported me throughout my studies.

Declaration of authorship

I hereby declare that I am the sole author responsible for this thesis. No source that is not in the list of references was used. Amongst others, figures and phrases that are taken directly from someone elses work are clearly indicated as such. Any figure that does not include a source has been made by myself. No passage was written using artificial intelligence or LLMs.

Kaiserslautern, Sep. 14, 2026
Place and date

K. Lüst
Signature

References

[1] S. N. Bose. Plancks Gesetz und Lichtquantenhypothese. *Zeitschrift für Physik*, 26(1):178–181, 1924.

[2] E. Busley, L. E. Miranda, A. Redmann, C. Kurtscheid, K. K. Umesh, F. Vewinger, M. Weitz, and J. Schmitt. Compressibility and the equation of state of an optical quantum gas in a box. *Science*, 375:1403, 2022.

[3] F. Dörr. *Dye Lasers*. Topics in Applied Physics. Springer Berlin, 1977.

[4] A. Einstein. Strahlungsemission und -absorption nach der Quantentheorie. *Verhandlungen der Deutschen Physikalischen Gesellschaft*, 18:318, 1916.

[5] A. Einstein. Quantentheorie des einatomigen idealen Gases. Zweite Abhandlung. *Sitzungsberichte der Königlich Preußischen Akademie der Wissenschaften (Berlin), Physikalisch-Mathematische Klasse*, pages 3–14, 1925.

[6] E. Busley et al. Supplementary materials for compressibility and the equation of state of an optical quantum gas in a box. *Science*, 375:1403–1406, 2022.

[7] T. Fließbach. *Statistische Physik: Lehrbuch zur Theoretischen Physik IV*. Springer, Heidelberg, 6. edition, 2018.

[8] W. Gerlach and O. Stern. Der experimentelle Nachweis der Richtungsquantelung im Magnetfeld. *Zeitschrift für Physik*, 9:349–352, 1922.

[9] R. C. Gilmore. *A Reexamination of the Kennard-Stepanov Relation*. PhD thesis, Department of Physics and Astronomy, University of Rochester, 1994.

[10] E. H. Kennard. On the thermodynamics of fluorescence. *Phys. Rev.*, 11:29, 1918.

[11] J. Klaers, J. Schmitt, T. Damm, F. Vewinger, and M. Weitz. Bose–Einstein condensation of paraxial light. *Applied Physics B*, 105:17–33, 2011.

[12] J. Klaers, J. Schmitt, F. Vewinger, and M. Weitz. Bose-Einstein condensation of photons in an optical microcavity. *Nature*, 468:545, 2010.

[13] J. Krauß, E. Stein, and A. Pelster. From lasers to photon Bose–Einstein condensates: A unified description via an open-dissipative Bose–Einstein distribution. *Eur. Phys. J. Spec. Top.*, 235:4311, 2026.

[14] W. Pauli. The Connection Between Spin and Statistics. *Physical Review*, 58:716–722, October 1940.

[15] Axel Pelster. Bose-Einstein-Kondensation. Vorlesungsskript, Fachbereich Physik, Universität Duisburg-Essen, July 2004.

[16] M. Pieczarka, M. Gębski, A. N. Piasecka, J. A. Lott, A. Pelster, M. Wasiak, and T. Czyszanowski. Bose–Einstein condensation of photons in a vertical-cavity surface-emitting laser. *Nature Photonics*, 18:1090–1096, 2024.

[17] J. Schmitt, M. Weitz, and J. Klaers. Absorption and emission spectral data of room-temperature rhodamine 6G dye solution and some typical dye microcavity parameters, 2024.

[18] R. C. Schofield, M. Fu, E. Clarke, I. Farrer, A. Trapalis, H. S. Dhar, R. Mukherjee, J. Heffernan, F. Mintert, R. A. Nyman, and R. F. Oulton. Bose–Einstein condensation of light in a semiconductor quantum well microcavity. *Nature Photonics*, 18:1083, 2024.

[19] E. Schrödinger. Quantisierung als Eigenwertproblem. *Annalen der Physik*, 384:361–376, 1926.

[20] E. Stein. Open-dissipative mean-field theory for photon Bose-Einstein condensates. Diplomarbeit, Fachbereich Physik, Technische Universität Kaiserslautern, July 2018.

[21] B. I. Stepanov. Universal relation between the absorption spectra and luminescence spectra of complex molecules. *Dokl. Akad. Nauk SSSR*, 112:839, 1957.

[22] B. I. Stepanov and V. P. Gribkovskii. *Theory of Luminescence*. Iliffe Books Ltd, London, 1968.

[23] M. Weitz. Calorimetry of a Bose-Einstein-condensed photon gas. Talk at "Quantum Fluids of Light and Matter", 2018.

List of Figures

1.1 Experimental set-up of harmonic trap. . . . 2
2.1 Experimental set-up of box trap. . . . 4
2.2 Sketch of mirror surface roughness. . . . 4
2.3 Sketch of photon dispersion within optical micro cavity. . . . 14
2.4 Rhodamine 6G emission and absorption spectrum. . . . 14
2.5 Sketch comparing thermal wavelength λ_{th} and particle distance d. . . . 14
3.1 Sketch of infra-red cut-off k_0 for analytical description. . . . 17
3.2 Thermal photons $N_{\mathrm{th}}(\mu)$ for different infra-red cut-offs. . . . 19
3.3 Thermal $N_{\mathrm{th}}(N)$ and ground-state photons $N_{0,0}(N)$ for different infra-red cut-offs. . . . 19
3.4 Total photon number $N(\tilde{\mu})$ and ground-state $N_{0,0}(\tilde{\mu})$ photons for periodic boundary conditions. . 21
3.5 **a)** $N_{\mathrm{th}}(N)$ and $N_{0,0}(N)$ for periodic boundary conditions. **b)** Convergence of critical particle number N_{c} dependent on maximum mode count. . . . 22
3.6 Thermal and ground-state particles plotted against N for varying L considering periodic boundary conditions. . . . 23
3.7 Behavior of N_{c} for large L considering periodic boundary conditions. . . . 24
3.8 Shifted chemical potential for the total particle number $\tilde{\mu}(N)$ and ground-state particles $\tilde{\mu}(N_{1,1})$ considering Dirichlet boundary conditions. . . . 25
3.9 Total photon number $N(\tilde{\mu})$ and ground-state $N_{1,1}(\tilde{\mu})$ photons for Dirichlet boundary conditions. . 25
3.10 $N_{1,1}(N)$ and $N_{\mathrm{th}}(N)$ compared to Heaviside functions considering Dirichlet boundary conditions for $L = 20\,\mu\mathrm{m}$. . . . 26
3.11 $N_{1,1}(N)$ and $N_{\mathrm{th}}(N)$ compared to Heaviside functions considering Dirichlet boundary conditions for multiple lengths. . . . 26
3.12 Comparison of analytical solution to closed system numerics for **a)** Dirichlet boundary conditions and **b)** periodic boundary conditions. . . . 28
3.13 Comparison of scalar c_0 for the IR cut-off k_0 for different L considering Dirichlet and periodic boundary conditions. . . . 28
4.1 Einstein coefficients of absorption ($B_{12}(E)$) and stimulated emission ($B_{21}(E)$) plotted against photon energy E. . . . 30
4.2 Cavity losses $\Gamma_{\mathrm{c}}(E)$ plotted against photon energy E. . . . 30
4.3 Total cavity photons depending on pumping rate p for $L = 40\,\mu\mathrm{m}$ and $\Gamma_{\mathrm{c}} = 4.00\,\mathrm{GHz}$. . . . 31
4.4 Molecular occupation for **a)** ground-state molecules and **b)** excited molecules. Considered is $L = 40\,\mu\mathrm{m}$. . . . 32
4.5 Solutions of the rate equations for different considered mode counts and $L = 40\,\mu\mathrm{m}$. . . . 32
4.6 Convergence of the critical particle number N_{c} dependent on mode count for **a)** $L = 20\,\mu\mathrm{m}$ and **b)** $L = 40\,\mu\mathrm{m}$. . . . 33
4.7 Numerical solutions to the rate equations for $L = 20\,\mu\mathrm{m}$. . . . 34
4.8 Chemical potential plotted against the system particle number for **a)** $L = 40\,\mu\mathrm{m}$ and **b)** $L = 20\,\mu\mathrm{m}$. 34
4.9 Critical particle number determined for different cavity losses considering a box length of $L = 20\,\mu\mathrm{m}$. The inset depicts the same for $L = 10\,\mu\mathrm{m}$. . . . 35
4.10 Behavior of the system for varying non-radiative losses Γ_{nr} in regards to **a)** the pumping rate and **b)** the critical particle number. . . . 36
4.11 Thermal and ground-state particles dependent on N for different Γ_{nr}. . . . 36